

Review

Prospective Obstacles and Improvement Strategies of Manganese-Based Materials in Achieving High-Performance Rechargeable Zinc–Air Batteries

Zhangli Ye, Tianjing Wu ^{*}, Lanhua Yi and Mingjun Jing ^{*}

The College of Chemistry, Xiangtan University, Xiangtan 411105, China

^{*} Correspondence: twu@xtu.edu.cn (T.W.); jingmingjun@xtu.edu.cn (M.J.)

Abstract

Zinc–air batteries (ZABs) are crucial for renewable energy conversion and storage due to their cost-effectiveness, excellent safety, and superior cycling stability. However, developing efficient and affordable bifunctional electrocatalysts for the oxygen reduction reaction (ORR) and the oxygen evolution reaction (OER) at the air cathode remains a significant challenge. Manganese (Mn)-based materials, known for their tunable oxidation states, adaptable crystal structures, and environmental friendliness, are regarded as the most promising candidates. This review systematically summarizes recent advances in Mn-based bifunctional catalysts, concentrating on four primary categories: Mn–N–C electrocatalysts, manganese oxides, manganates, and other Mn-based compounds. By examining the intrinsic merits and limitations of each category, we provide a comprehensive discussion of optimization strategies, which include morphological modulation, structural engineering, carbon hybridization, heterointerface construction, heteroatom doping, and defect engineering, aimed at enhancing catalytic performance. Additionally, we critically address existing challenges and propose future research directions for Mn-based materials in rechargeable ZABs, offering theoretical insights and design principles to advance the development of next-generation energy storage systems.



Academic Editor: Sylvain Franger

Received: 4 June 2025

Revised: 3 July 2025

Accepted: 7 July 2025

Published: 8 July 2025

Citation: Ye, Z.; Wu, T.; Yi, L.; Jing, M. Prospective Obstacles and Improvement Strategies of Manganese-Based Materials in Achieving High-Performance Rechargeable Zinc–Air Batteries. *Batteries* **2025**, *11*, 255. <https://doi.org/10.3390/batteries11070255>

Copyright: © 2025 by the authors. Licensee MDPI, Basel, Switzerland. This article is an open access article distributed under the terms and conditions of the Creative Commons Attribution (CC BY) license (<https://creativecommons.org/licenses/by/4.0/>).

1. Introduction

Rechargeable zinc–air batteries (ZABs) are emerging as a critical research focus within the future energy landscape due to their exceptional theoretical energy capacity (up to 1086 Wh kg^{-1}), cost-effectiveness, inherent operational safety, coupled with excellent cyclability during charge–discharge cycles, and the widespread availability of zinc raw materials globally [1]. However, the large-scale application of the current state-of-the-art ZABs is still hindered by several challenges, such as the deactivation and degradation of oxygen electrocatalysts, corrosion and passivation of zinc, as well as consumption and carbonization of the electrolyte [2–4]. Consequently, more efforts are required, including the development of efficient oxygen electrocatalysts, suppression of corrosion and dendrite growth on the zinc anode, and optimization and modification of the electrolyte, to enhance the reversibility of electrochemical redox reactions in rechargeable ZABs (Figure 1a). A typical rechargeable ZAB consists of four main components: a zinc anode, an air cathode, a liquid electrolyte, and a separator. The electrochemical reactions occurring at the two electrodes are as follows [5,6]:

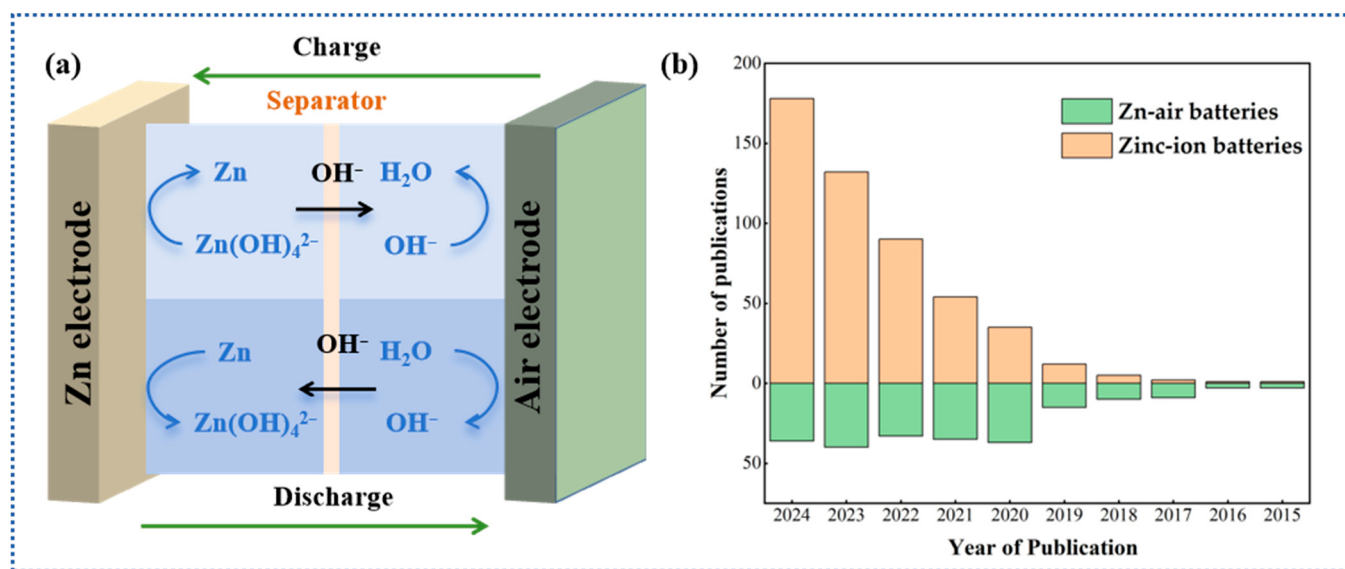
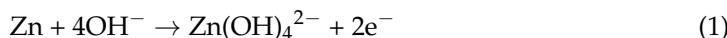


Figure 1. (a,b) A comparative plot illustrating the number of publications on zinc–air batteries and zinc-ion batteries over the past decade.

Anode reaction of zinc:



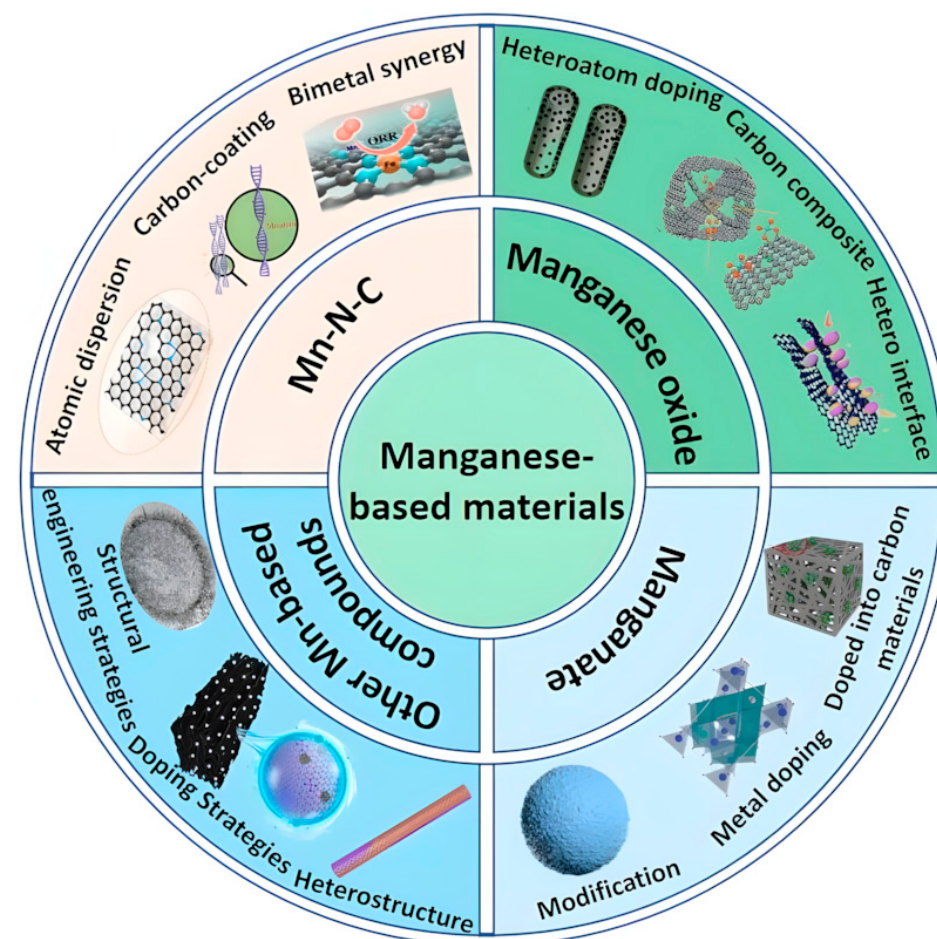
Cathode reaction of air:



The anode reaction of zinc is a two-step process. During discharge, zinc is first oxidized to form soluble zincate ions ($Zn(OH)_4^{2-}$). When the electrolyte becomes supersaturated, the zincate ions decompose into insoluble ZnO . Meanwhile, at the air cathode, oxygen from the atmosphere diffuses into the gas diffusion layer and is immediately reduced to hydroxide ions upon contact with the alkaline electrolyte. During charging, the electrochemical reactions are reversed, with zinc metal being deposited from the aqueous electrolyte and oxygen being evolved and diffused out. However, the development of rechargeable ZABs is limited by the lack of robust and cost-effective catalysts to efficiently drive the ORR and OER at the air cathode [7,8].

Contemporary research on cathode catalysts for rechargeable ZABs predominantly focuses on two paradigms: noble metal-based and non-noble metal-based catalysts. While noble metal catalysts (e.g., IrO_2 , RuO_2 , Pt/C) exhibit superior electrocatalytic activity, their practical deployment is hindered by prohibitive costs, resource depletion risks, suboptimal selectivity, and compromised long-term durability under operational conditions [9,10]. In contrast, non-noble metal catalysts, particularly transition metal-based materials, demonstrate exceptional properties attributed to their variable oxidation states stemming from incompletely filled d-orbitals, superior electrical conductivity, and abundant active defect sites [11–13]. Among these, manganese-based catalysts exhibit promising application prospects in rechargeable ZABs due to the low reactivity of Mn^{2+} with H_2O_2 , which effectively mitigates the Fenton reaction [14]. Moreover, their diverse oxidation states, crystalline structures, high catalytic activity, environmental compatibility, cost-efficiency, compositional versatility, and scalability collectively underscore their extensive applicability in rechargeable ZABs.

Although significant advances have been made in the development of manganese-based electrocatalysts for rechargeable ZABs, the existing literature predominantly focuses on their applications in alternative electrochemical systems, such as zinc-ion batteries, as shown in Figure 1b. As a result, there is a notable gap in the systematic summarization of catalytic mechanisms and optimization strategies tailored for rechargeable ZABs. This review delineates the research progress of manganese-based materials as air cathodes in rechargeable ZABs, categorizing them into four distinct classes (Scheme 1): Mn–N–C electrocatalysts, manganese oxides, manganates, and novel Mn-based compounds. For each material category, the unique characteristics, inherent limitations, and optimization strategies of Mn-based electrocatalysts are critically analyzed. Additionally, this review highlights the existing challenges, future development trends, and research prospects of Mn-based materials in rechargeable ZABs. By elucidating these aspects, the study aims to provide actionable insights for researchers, thereby accelerating the efficient advancement of rechargeable ZABs in energy storage applications.



Scheme 1. Common classes of manganese-based materials and their corresponding modification strategies for enhanced electrocatalytic performance.

2. Mn–N–C Electrocatalysts

Mn-based materials, either in metallic form or alloyed with other elements and encapsulated within nitrogen-doped porous carbon frameworks (denoted as Mn–N–C electrocatalysts), have demonstrated significant potential as oxygen electrocatalysts for rechargeable ZABs. This is ascribed to their high specific surface area, three-dimensionally interlinked conductive network, and remarkable stability in alkaline electrolyte environments. Within this configuration, the N-doped carbon matrix demonstrates dual functionality, serving

as both an efficient conductive network for electron transfer and a structural separator preventing manganese species accumulation. This synergistic mechanism facilitates the homogeneous dispersion of catalytically active Mn centers throughout the composite architecture. Additionally, heteroatom doping introduces synergistic catalytic sites that further enhance electrocatalytic performance. Based on the structural attributes of active sites and the configuration of Mn species, Mn–N–C catalysts are systematically categorized into two discrete classes, which will be comprehensively delineated in the subsequent analysis.

2.1. Atomic Mn–N_x–C

With the evolution of nanotechnology and advancements in catalyst characterization methodologies, surface atoms bearing unsaturated coordination configurations have been conclusively identified as the predominant active sites in heterogeneous catalytic reactions. Through the judicious control of the grain dimensionality, morphological architecture, and the exposed crystal facet ratios of catalytic materials, the topological arrangement and coordination environment of surface atoms can be strategically engineered to optimize catalytic efficacy. Notably, as catalyst architectures approach atomic-scale dimensions through cluster formation or isolated atomic distribution, the electronic configurations and reactive properties of Mn–N_x–C-based systems demonstrate substantial modifications. This reduction enables the maximal utilization of the active material by exposing isolated Mn–N_x coordination units, which synergistically optimize the adsorption/desorption kinetics of critical reaction intermediates and stabilize key reaction intermediates. Consequently, the catalyst demonstrates a marked enhancement in both electrocatalytic activity and operational stability. Currently, the synthetic strategies for atomic Mn–N_x–C catalysts predominantly encompass precursor engineering, coordination environment modulation, and spatial confinement techniques. These methodologies collectively stabilize the atomic dispersion of metal centers at the nanoscale, thereby effectively mitigating the propensity for metal atom migration across the carbonaceous substrate.

Morphological, structural, and functional regulation of Mn–N_x–C catalysts can be achieved through systematic modulation of precursor chemistry, reaction pathways, and transformation conditions. Specifically, atomic Mn–N–C catalysts are synthesized through a sequential adsorption–thermal decomposition strategy, utilizing bimetallic Mn/Zn-ZIF precursors with tailored topological frameworks. Significantly, the high-temperature-induced Zn volatilization from ZIF skeletons inhibits Mn nanoparticle coalescence, thereby facilitating the generation of atomically dispersed Mn–N_x moieties coordinated with nitrogen-based donors. Subsequent NH₃ activation (designated as Mn–N–C (2.0)) introduces carbon lattice defects, significantly increasing specific surface area ($1557\text{ m}^2\text{ g}^{-1}$) and microporosity (Figure 2a). This hierarchical architecture maximizes exposure of reactive Mn single-atom sites, conferring exceptional ORR activity in alkaline electrolytes [15]. Beyond MOF-derived precursors, salt-assisted templating strategies have emerged as a complementary approach for carbon structural engineering and single-atom site implantation. Li et al. [16] successfully fabricated Mn single-atom catalysts (MnSAs) anchored on nitrogen-doped mesoporous carbon (NMC) nanosheets via a salt-templated strategy, demonstrating that MnCl₂ acts as a bifunctional mediator for hierarchical pore formation and morphological tuning. The resulting MnSAs/NMC composite exhibits a highly interconnected mesoporous framework with abundant accessible active sites, facilitating efficient electron/ion diffusion pathways (Figure 2b). When utilized as the cathode material in rechargeable ZABs, the MnSAs/NMC-based rechargeable ZABs exhibit an open-circuit voltage (OCV) of 1.52 V, attains a peak power density of 210.3 mA cm^{-2} under a specified current density, and presents a specific capacity of 842 mAh g^{-1} . These performance metrics collectively outperform those of a rechargeable ZABs employing a Pt/C-based cathode.

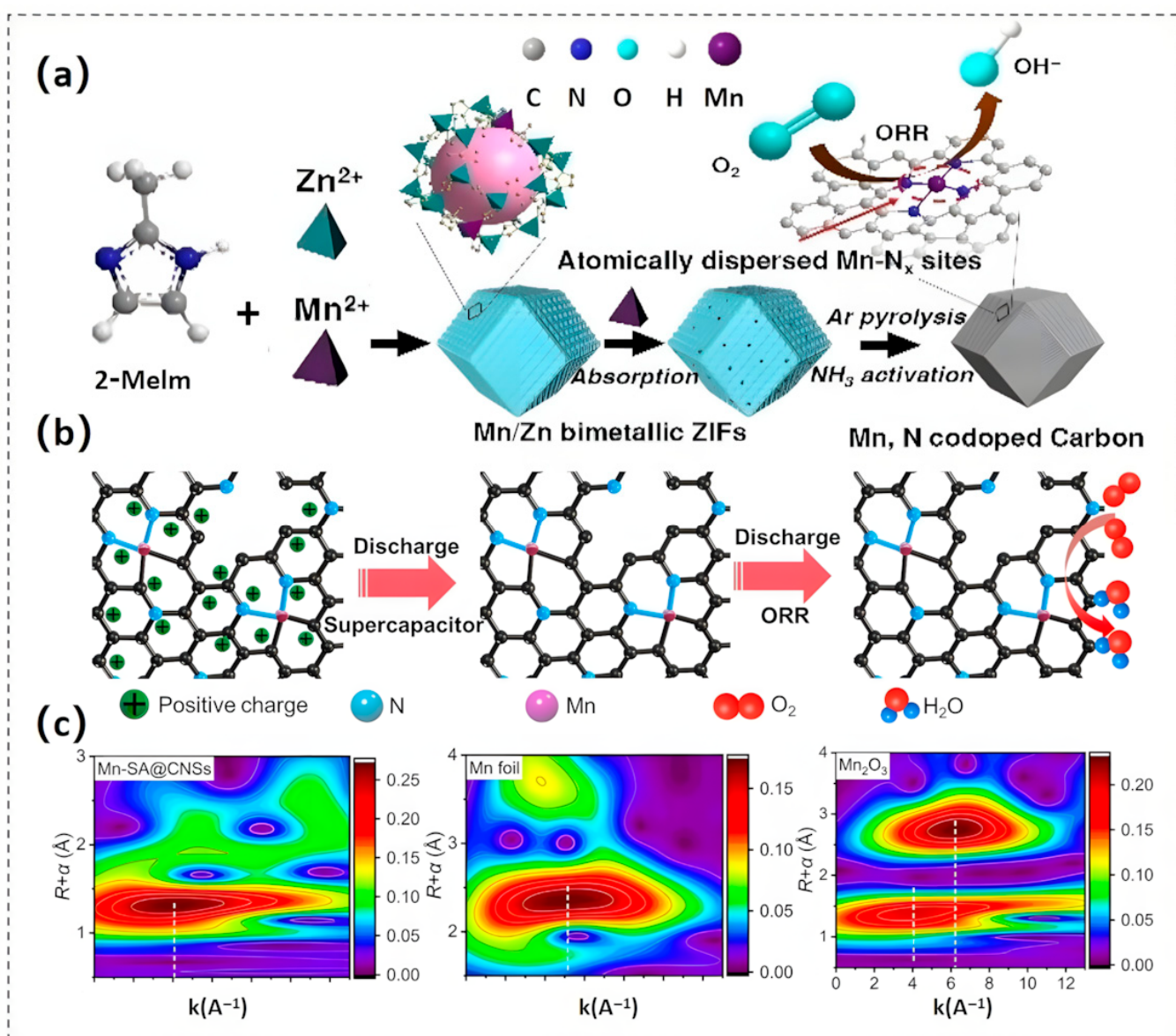


Figure 2. (a) Schematic illustration showcasing the synthesis process of the Mn-N-C electrocatalyst. Reproduced with permission [15]. Copyright 2021 Wiley-VCH GmbH. (b) Graphical representation illustrating the parallel discharge mechanism of “supercapacitor + ORR” within the MnSAs/NMC-based Zn-air battery. Reproduced with permission [16]. Copyright 2024 Elsevier. (c) EXAFS spectra analysis of Mn-SA@CNSs along with their reference specimens. Reproduced with permission [17]. Copyright 2022 Elsevier.

In addition to the previously mentioned engineering approaches, heteroatomic species such as nitrogen, sulfur, phosphorus, and oxygen can serve as stable coordination sites for metal atoms. This capability facilitates the rational design of atomically dispersed Mn-N_x-C catalysts by enhancing interactions between the metal and the support (as illustrated in Figure 2c). For example, by tailoring the N/O coordination microenvironments, researchers can engineer the atomic-level electron delocalization of the d-orbitals in manganese single-atom (Mn-SA) centers [17]. Theoretical calculations based on DFT reveal that transitioning the coordination environment of Mn-SA centers from exclusive nitrogen coordination Mn-(N-C₂)₄ to hybrid N/O-coordinated Mn-(N-C₂)₂(O-C₂)₂ configuration modifies the electronic distribution of the d-orbitals. This alteration consequently affects the binding energies of the ORR intermediates at the catalytic Mn-SA sites. The electronic reconfiguration resulting from N/O dual-ligand coordination significantly reduces the ki-

netic barrier for oxygen reduction, allowing Mn-SA@CNSs catalysts to achieve exceptional electrocatalytic performance in the ORR.

Unlike traditional methods that introduce Mn single atoms through precursors and coordinate them with heteroatoms, the spatial confinement strategy takes advantage of the unique architecture of molecular cages to securely anchor metal atoms in a confined space (Table 1). This approach effectively restricts their movement and prevents aggregation. For example, the ZIF-8 nanocages possess intrinsic spatial confinement properties that facilitate the efficient trapping of individual Mn(acac)₃ molecules within their internal cavities, as demonstrated by Xu and his team [4]. This methodology significantly reduces manganese agglomeration during thermal treatment by enhancing thermodynamic coordination with nitrogen dopants, which optimizes the stabilization process for creating Mn-N_x catalytic sites. Structural characterization and performance evaluations confirmed that the atomically dispersed Mn-N-C-900 material exhibited exceptional ORR kinetics and electrochemical durability.

Table 1. ORR performance and ZAB metrics of reported atomic Mn–N_x–C catalysts.

Electrocatalysts	Loading [Mn Atoms]	ORR		Performance (ZABs)			Ref.
		E _{1/2} [V]	OCV [V]	Specific Capacity [mAh·g ⁻¹]	Peak Power Density [mW cm ⁻²]	Stability	
Mn-N _x C (2.0)	0.035 wt%	0.885	1.53	828.1	116.6	3000 cycles 200 h@ 10 mA cm ⁻²	[15]
MnSAs/NMC	1.61 wt%	0.9	1.52	842	210.3		[16]
MnNCS-4-800	0.20 wt%	0.89 (acidic) 0.71 (alkaline)	1.51	796.43	233	-	[18]
MnSA-MnP-980	-	0.88	-	-	51	27 h@2 mA cm ⁻²	[19]
Mn-N-C-35	1.71 wt%	0.92 (acidic) 0.78 (alkaline)	-	655	176	250,000 s cycle test at 10 mA cm ⁻²	[20]
Mn-N ₂ S ₂ -C	0.7 wt%	0.91	1.51	780.4	193	250 h@10 mA cm ⁻²	[21]
Mn-N ₃ -O	-	0.900	1.53	-	210	>350 h@10 mA cm ⁻²	[22]
Mn/NDC	0.2 wt%	-	1.48	1.29	268.5	>1600 h@20 mA cm ⁻²	[23]
Mn-N-P-C	1.54 wt%	0.82	1.45	830	133	-	[24]
Mn@NC-900	1.17 wt%	0.900	1.33	-	118	20,000 s	[25]
Mn-N-C	-	0.87	1.55	-	141	100 h@10 mA cm ⁻²	[26]

2.2. Mn-Based Alloys Confined in N-Doped C

The integration of manganese-based alloys, such as MnFe and MnCo, enhances the modulation of their electronic structure, improves electron conduction efficiency, and increases the density of active sites for reversible oxygen electrocatalysis. The geometric architectures of the Mn–AMA active sites (with AMA representing another metallic component, such as Fe or Co) can be categorized into two main structures: (1) an isolated bimetallic site structure that features both Mn-N₄ and AMA-N₄ moieties; and (2) a bridged bimetallic bonding structure, where direct coordination between manganese and ANA creates a Mn-AMA dimer, resulting in an N₃-Mn-AMA-N₃ coordination geometry.

Experimental and theoretical investigations have demonstrated that Fe-N moieties exhibit optimal adsorption/desorption energies during catalytic processes, conferring exceptional ORR activity and OER performance (in Table 2). Consequently, MnFe-N-C materials have been engineered to exploit the synergistic coupling of Fe-N_x and Mn-N_x active centers for enhanced electrocatalysis. To illustrate, Chen and colleagues synthesized a Mn-Fe bimetallic dual-site catalyst (Fe/Mn-N_x-C/NC) with isolated active sites, revealing a Mn-Fe cooperative cascade mechanism for O₂ activation [27]. Specifically, Fe sites facilitate O₂ protonation to form *OOH and *O, followed by *OH transfer to adjacent Mn-N_x sites, thereby optimizing activity by mitigating weak *OH binding at single-metal sites (Figure 3a). The activation energy barrier for this pathway is significantly lower than that of isolated Fe-N_x or Mn-N_x sites, surpassing Pt/C in ORR activity and exhibiting superior rechargeable ZAB performance. To optimize catalytic performance, a high-activity FeMn-N/S-C-1000 catalyst was developed by incorporating dual heteroatoms (N/S) into a carbon-based framework through high-temperature pyrolysis [28]. The catalytic core of the FeMn-N₅/S-C configuration demonstrates superior inherent activity toward both ORR/OER, serving as the principal active site for bifunctional electrocatalytic processes. The N/S co-doping strategy expands the surface area, enhances active site dispersion, and modulates the electronic structures of Fe and Mn, thus accelerating reaction kinetics. Furthermore, the N₃-Mn-Fe-N₃ configuration exhibits remarkable performance in rechargeable ZABs. The carbon-based catalyst co-doped with Fe, Mn, and N, synthesized through pyrolysis of fish gill biomass (designated as Fe, Mn, N-FGC), exhibits pronounced pH-universal oxygen reduction performance. This catalytic capability facilitates exceptional operational stability in rechargeable ZAB applications, obtaining a maximum power output of 220 mW cm⁻² under alkaline conditions. Spectroscopic and computational analyses reveal that the π-electron repulsion between adjacent Fe²⁺ centers within the Fe-Mn bimetallic pair modulates the electronic structure of Mn²⁺, leading to strengthened π-conjugation interactions. This electronic tuning stabilizes the 3C-2e⁻ oxygen intermediate bond, thereby promoting enhanced O₂ adsorption and activation at the heteronuclear catalytic sites (Figure 3b). Consequently, the energy barrier for ORR is significantly reduced versus monometallic Mn-N-C counterparts [29].

The unique electronic configuration of cobalt (featuring partially occupied d-orbitals) endows it with exceptional coordination capability toward organic ligands, enabling its effective encapsulation within zeolitic imidazolate frameworks (ZIFs). Leveraging the ZIF architecture, Chao's research group synthesized bimetallic Mn-Co and nitrogen co-doped carbon matrix catalyst (MnCo-N-C) for ORR, demonstrating a synergistic catalytic mechanism mediated by atomically dispersed CoN_x and MnN_x sites acting as dual active centers [30]. Mechanistic investigations revealed that, in contrast to monometallic Co-N-C catalysts, the MnCo-N-C catalyst optimizes ORR kinetics through modulated electronic distribution between Mn and Co. This modulation enhances the adsorption of the *OOH intermediate, promoting the 4e⁻ ORR pathway, while concurrently weakening the binding of the *O₂ intermediate to mitigate oxidative attack from H₂O₂, thereby enhancing the catalyst's durability (Figure 3c,d). Furthermore, the atomic-scale configuration of Mn-Co bimetal centers may adopt a coordination architecture where manganese and cobalt atoms establish covalent linkages within nitrogen-rich porous carbon matrices, forming N₃-Mn-Co-N₃ moieties. DFT calculations unveiled that this configuration facilitates a –O–O– bridged adsorption model, accelerating O–O bond cleavage thus promoting an efficient 4e⁻ transfer reaction. Additionally, the cooperative interaction between Mn and Co active centers provides two anchoring sites conducive to metal–oxygen bond formation, thereby lowering the activation energy of the rate-limiting O₂ activation step.

and expediting ORR kinetics. Consequently, the MnCo-N-C catalyst shows remarkable ORR kinetics in proton-conducting electrolytes [31].

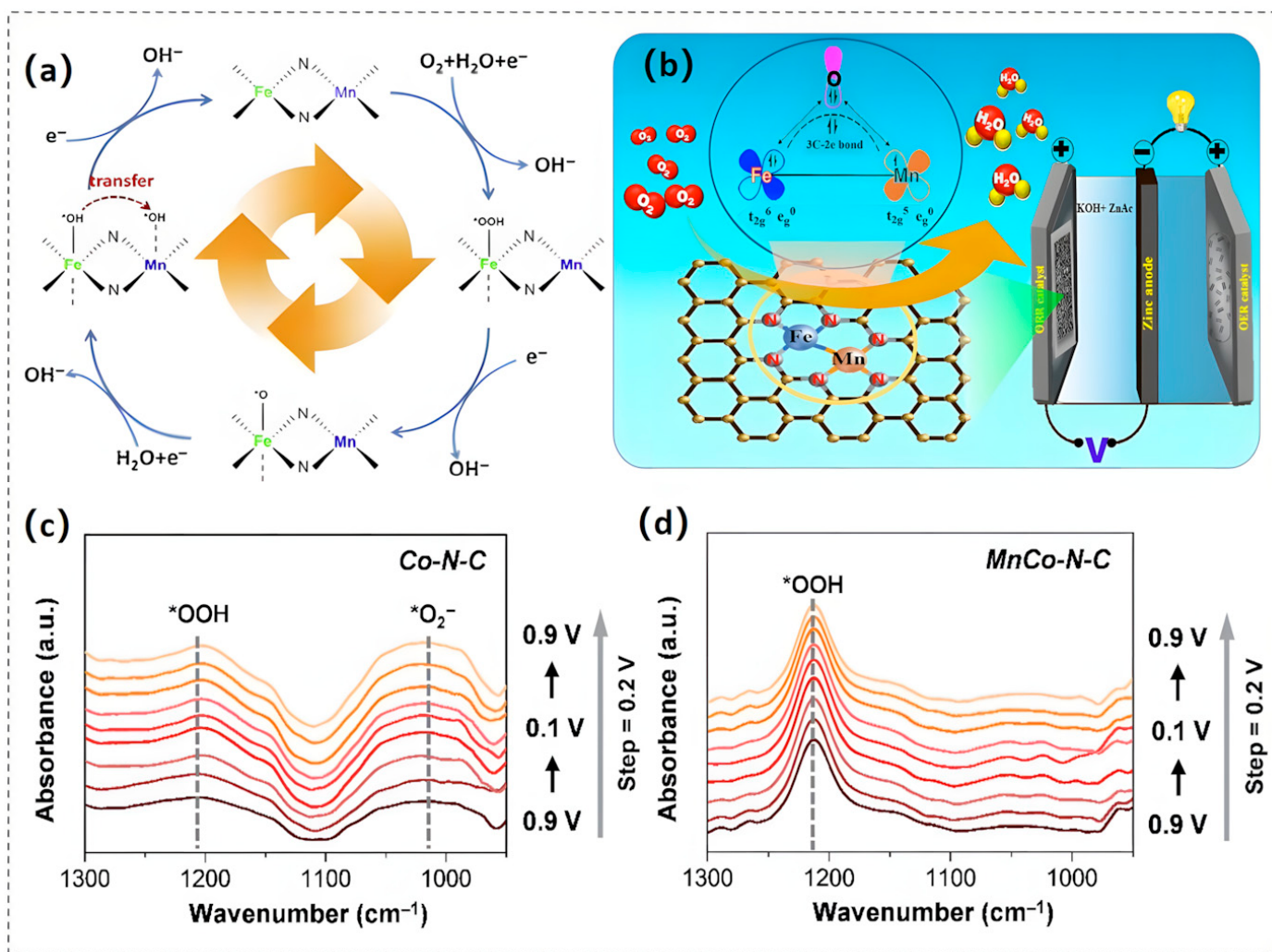


Figure 3. (a) Mechanistic diagram of the cascade reaction mechanism mediated by FeN_x and MnN_x sites. Reproduced with permission [27]. Copyright 2021 Elsevier. (b) Structural representation of the Fe, Mn, N-FGC catalyst for Zn-air batteries. Reproduced with permission [29]. Copyright 2020 American Chemical Society. (c,d) In situ ATR-SEIRAS spectra of Co-N-C (c) and MnCo-N-C (d) catalysts. Reproduced with permission [30]. Copyright 2022 The Royal Society of Chemistry.

Table 2. Electrocatalytic ORR performance and ZABs of Mn-based alloys confined in N-doped carbon.

Electrocatalysts	ORR		Performance (ZABs)			Ref.
	$E_{1/2}$ [V]	OCV [V]	Specific Capacity [mAh g^{-1}]	Peak Power Density [mW cm^{-2}]	Stability	
Fe/Mn-N _x -C	0.88	-	-	208.6	>18 h@10 mA cm ⁻²	[27]
FeMn-N/S-C-1000	0.924	1.45	-	346	90 h@10 mA cm ⁻²	[28]
CoMn/NC	0.82 (acidic) 0.89 (alkaline)	1.487	-	176	>30 h@40 mA cm ⁻²	[31]
Fe/Mn-N/C	0.891	1.35	-	178.18	-	[32]

Table 2. *Cont.*

Electrocatalysts	ORR		Performance (ZABs)			Ref.
	$E_{1/2}$ [V]	OCV [V]	Specific Capacity [mAh g ⁻¹]	Peak Power Density [mW cm ⁻²]	Stability	
Z-Fe1Mn1-NC	0.80 (acidic) 0.82 (alkaline)	1.475	596.0 –	164.3	–	[33]
PBA-MnCo-N-C	0.859	1.48	917.31	102.25	>167 h	[34]
FeMn ac/Mn-N ₄ C	0.79	1.46	–	207	100 h	[35]
Co ₃ Fe ₇ /N, Mn-PC	0.87	–	–	–	2000 cycles	[36]
MnNC-PDA-700	0.87	–	760.2	122.7	10,000 cycles	[37]
Mn-Fe@NCNTs	0.80 (acidic) 0.872 (alkaline)	1.487	628.7	139.2	29,000 s	[38]
FeMn(mIm)-N-C	0.778 (acidic) 0.861 (alkaline)	1.518	–	160	20,000 s	[39]
FeMn-DSAC	0.922	1.45	–	184	80 h@ 2mA cm ⁻²	[40]
MnCoZn-NC	0.88	1.50	–	119.2	>150 h	[41]
MnCoNi-C-D	–	1.46	841.3	116.4	>180 h	[42]

3. Manganese Oxide

Manganese oxides, including MnO, MnO₂, Mn₃O₄, and Mn₂O₃, have been recognized as competitive bifunctional electrocatalysts for electrochemical reactions. This performance is attributed to their adaptable 3d electronic structures, varying polymorphic phases, and properties that can be tailored through modifications in morphology [43]. The related electrochemical performances are listed in Table 3. However, the inherent semiconductor characteristics of manganese oxides limit the accessibility of electroactive sites, hinder mass transport processes, and decrease charge mobility, which ultimately leads to suboptimal electrocatalytic efficiency. To address these challenges, researchers have developed several effective strategies. Among the most commonly used approaches are compositing with conductive materials, modifying morphology, fabricating heterostructures, and implementing doping modifications.

3.1. MnO

The rock-salt-type crystal structure of manganese oxide (MnO) is relatively stable, allowing it to maintain its structural integrity effectively. However, during prolonged charge–discharge cycling, MnO can undergo phase transformations or structural degradation, which may lead to a decline in its catalytic activity and electrical conductivity. To address these issues, researchers have developed various optimization strategies. One promising approach involves fabricating MnO-based composites using graphene derivatives and porous carbonaceous matrices, which have proven effective in enhancing electrochemical performance. Additionally, nitrogen doping can be used to adjust the electronic configuration and improve the inherent electronic conductivity of the material. In a notable study, a light-driven synthesis strategy was employed to prepare highly crystalline Mn₃O₄ nanoparticles [44]. Subsequently, these nanoparticles were anchored onto nitrogen-doped reduced graphene oxide (N-rGO) through a one-step calcination process. This innovative strategy effectively yielded a MnO/N-rGO composite electrocatalyst, which demonstrated exceptional catalytic performance. Electrochemical evaluations in alkaline media revealed an $E_{1/2}$ of 0.843 V for the hybrid material, accompanied by outstanding resistance to methanol crossover and significant durability over extended operational periods.

Moreover, the integration of additional metal (such as Co [45,46], Cu [47]) onto nitrogen-doped carbon-coated MnO presents a more efficient method for enhancing its dual-

functional oxygen electrocatalytic performance compared to single-component systems. Recent breakthroughs in core–shell-structured MnO@Cu-N-C nanorods have showcased remarkable bifunctional catalytic capabilities [47]. This excellent electrocatalytic behavior arises from the well-defined interfacial synergy inherent in the heterostructure design, which promotes efficient electron transport at the MnO-Cu-N-C junction interface. Concurrently, the architecture precisely modulates the binding energetics of critical oxygen intermediates ($^{\bullet}\text{O}$, $^{\bullet}\text{OH}$, $^{\bullet}\text{OOH}$) during adsorption and desorption processes, thereby optimizing reaction kinetics. As a direct consequence, these optimized kinetic processes accelerate the rates of the OER and the ORR (Figure 4a). The rechargeable ZABs assembled with this catalyst attained a peak power density of 196.8 mW cm^{-2} and exhibited stable charge–discharge cycling performance, sustaining over 650 h of cycling without significant performance degradation, as shown in Figure 4b.

Unlike the construction of composite materials, the engineering of metal/metal oxide heterointerfaces primarily focuses on enhancing catalytic performance through electronic effects, lattice matching, and chemical bonding at the interface [48,49]. As illustrated in Figure 4c, Ji and his team pioneered the controlled synthesis of Ni|MnO heterostructure interfaces embedded within porous carbon nanofiber matrices (Ni|MnO/CNF) by leveraging carboxyl-functionalized carbon nanotubes as reactive templates for stabilizing metal-ion precursors [50]. At the Ni|MnO heterointerface, Ni-Mn alloy nanobridges establish a covalent linkage that stabilizes the interface by reinforcing interfacial adhesion. This architecture inhibits catalyst particle coalescence through steric hindrance and suppresses activity decay by blocking grain boundary migration during electrochemical cycling. DFT calculations indicate that the formation of this interface triggers lattice distortion within the MnO sub-lattice. This distortion leads to an elongation of Mn-O bond lengths and a modification of the electronic configuration of Mn atoms. Nearby Ni atoms serve as electron-donating species, causing a downward shift in their d-band centers. The synergistic interplay between electronic redistribution and charge transfer mechanisms optimizes the thermodynamic stability of reactive intermediates adsorbed on catalytic surfaces, thereby conferring superior bifunctional activity.

3.2. MnO_2

Manganese dioxide (MnO_2), a pivotal member of the manganese oxide family, exhibits exceptional potential serving as a dual-functional electrocatalyst enabling OER/ORR, attributed to its tunable crystal structures, high intrinsic conductivity, and reversible redox kinetics. Its fundamental structural unit is the $[\text{MnO}_6]$ octahedron, which forms various crystal structures such as cryptomelane ($\alpha\text{-MnO}_2$), pyrolusite ($\beta\text{-MnO}_2$), and birnessite ($\delta\text{-MnO}_2$) through different stacking and connection patterns. $\alpha\text{-MnO}_2$ comprises two types of tunnel structures: $[2 \times 2]$ tunnels ($0.46 \text{ nm} \times 0.46 \text{ nm}$) and $[1 \times 1]$ tunnels ($0.23 \text{ nm} \times 0.23 \text{ nm}$) [51]. The $[2 \times 2]$ tunnel architecture, comprising corner- and edge-coordinated $[\text{MnO}_6]$ octahedra that form interconnected voids accommodating hydrated cations or solvent species, amplifies the electrochemically accessible surface area (EASA) through exposure to high-energy Mn sites and facilitates mass transport via ordered ion/molecule diffusion pathways within the periodic lattice [52]. $\beta\text{-MnO}_2$ exhibits a $[1 \times 1]$ tunnel framework constituted by edge-linked $[\text{MnO}_6]$ octahedral chains bridged via vertex sharing, yielding one-dimensional confined channels with restricted ionic accessibility. In contrast, $\delta\text{-MnO}_2$ adopts a layered structure stabilized by interlayer van der Waals interactions, enabling open interlayer galleries for facile ion intercalation and a high specific surface area [53]. Amorphous MnO_2 (AMO) lacks long-range order, with $[\text{MnO}_6]$ octahedra randomly cross-linked, resulting in a defect-rich and structurally heterogeneous electrocatalytic interface (Figure 5a). Electrocatalytic activity trends of MnO_2 polymorphs

in alkaline media exhibit structure-dependent hierarchy: α -MnO₂ (2×2 tunnels) surpasses AMO, β -MnO₂, and δ -MnO₂ in activity, attributed to its optimal balance between accessible surface sites and ionic conductivity [54]. However, this ranking is morphology- and electrolyte-sensitive, as the activity of MnO_x-based catalysts is further modulated by surface facet exposure, interlayer spacing, and alkali cation co-intercalation [53].

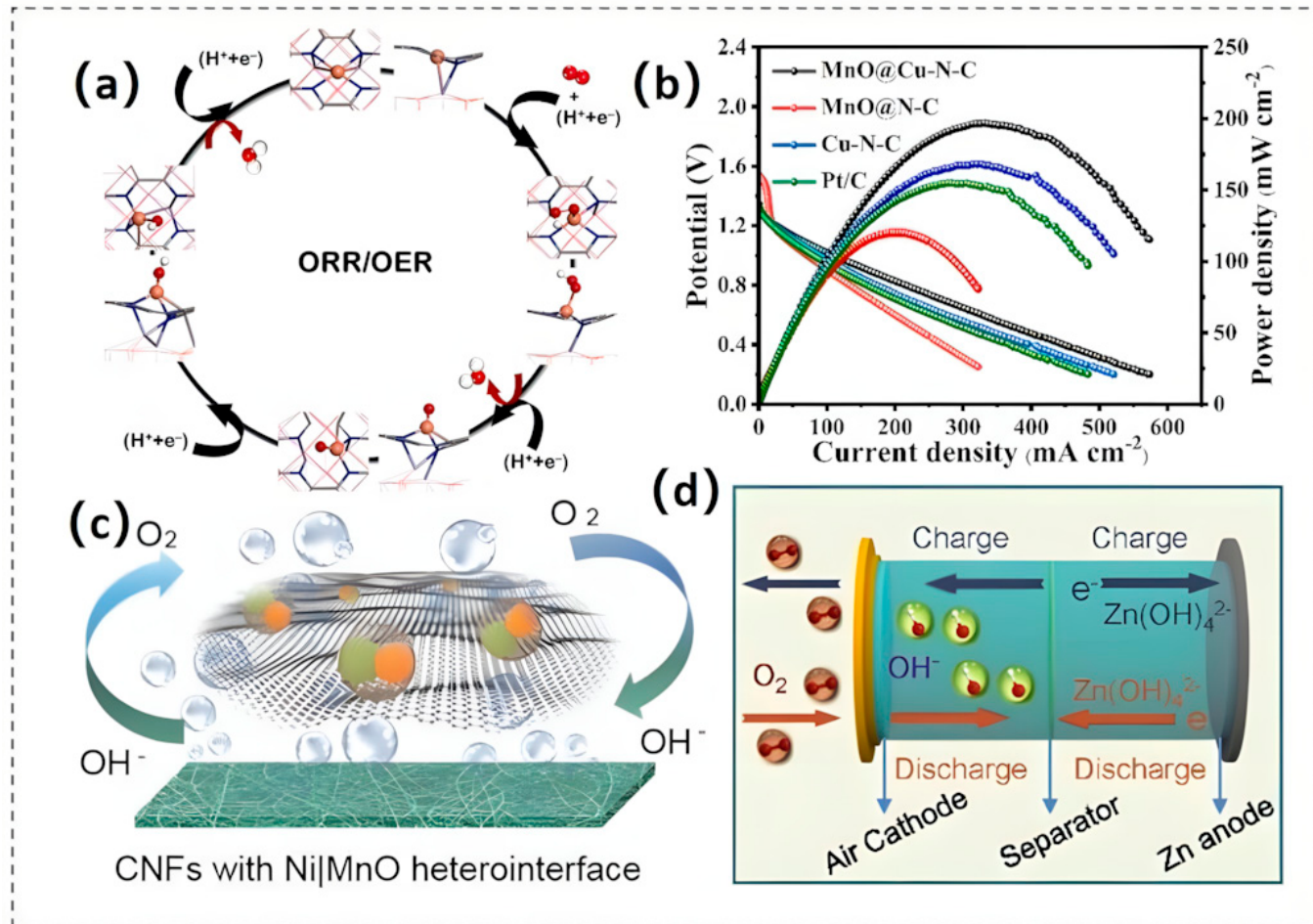


Figure 4. (a) Refined structural configurations (exhibiting both top and side perspectives) of the intermediates involved in the ORR and OER adsorbed onto the MnO@Cu-N-C substrate. (b) Polarization characteristics and power density profiles of the Zn-air battery utilizing MnO@Cu-N-C or Pt/C as the catalytic agent. Reproduced with permission [47]. Copyright 2022 Elsevier. (c) Depiction of Ni|MnO CNF serving as a dual-function oxygen catalyst. Reproduced with permission [50]. Copyright 2020 Wiley-VCH GmbH. (d) Diagrammatic layout of the Zn-air battery. Reproduced with permission [43]. Copyright 2022 Elsevier.

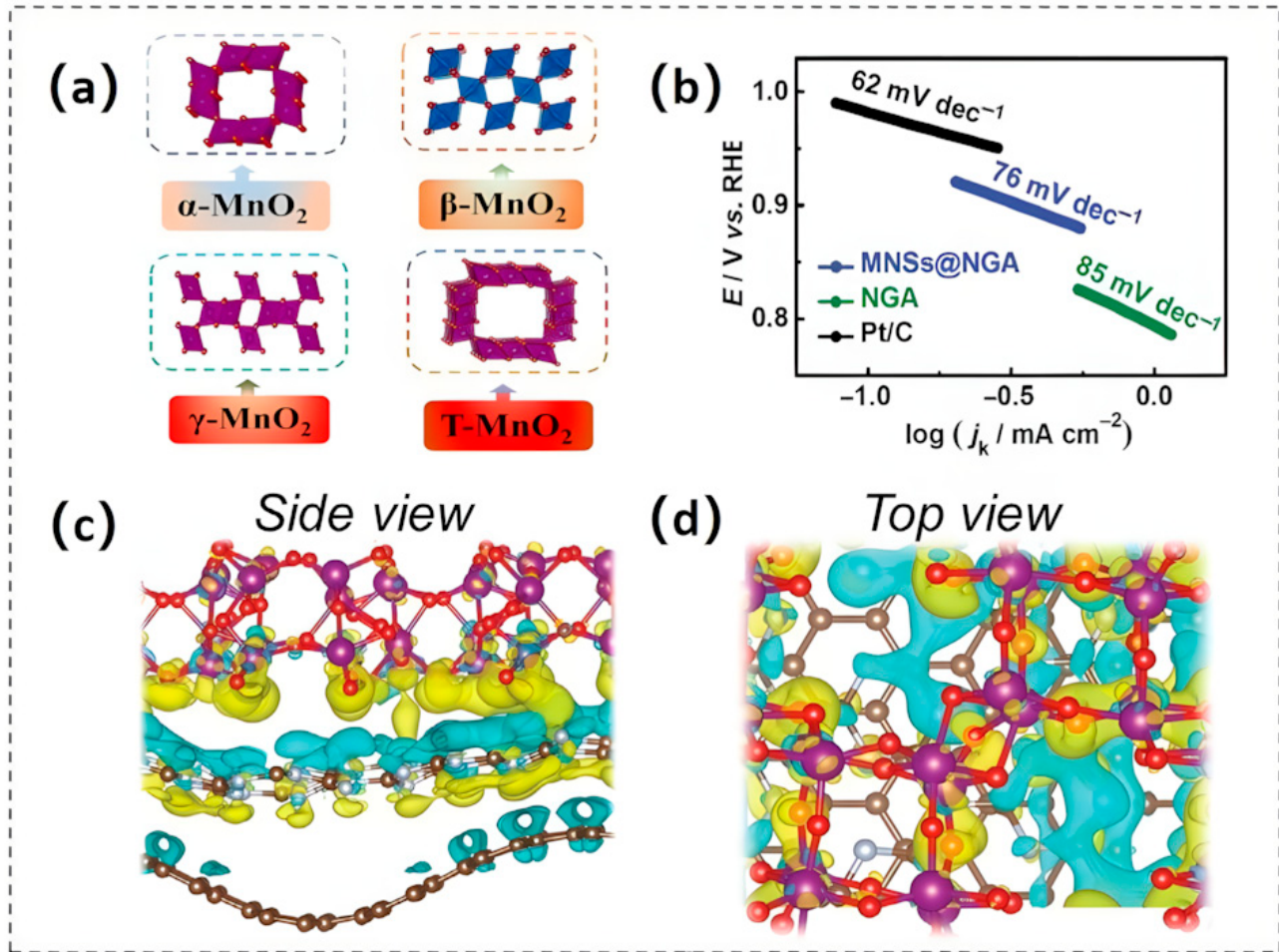


Figure 5. (a) The structures of the four types of MnO₂. (b) Tafel kinetics analysis for MNSs@NGA, NGA, and Pt/C catalysts. Reproduced with permission [55]. Copyright 2021 The Royal Society of Chemistry. Charge density disparities in (c) the lateral perspective and (d) the overhead perspective of MCC. Reproduced with permission [56]. Copyright 2024 Wiley-VCH GmbH.

MnO₂ exhibits low intrinsic electronic resistivity (10^{-5} – 10^{-6} S/cm), which imposes kinetic constraints on charge storage kinetics, particularly at high current densities. To address this issue, MnO₂ is often supported on conductive carbonaceous scaffolds (e.g., graphene sheets [57], carbon nanotube arrays [58], and carbon nanofiber networks) to engineer charge transfer pathways and enhance overall electrochemical utilization efficiency. Additionally, morphologically engineering MnO₂ at the nanoscale can optimize charge transport and enhance mass transfer capabilities. For instance, a study presented a hierarchical aerogel composite comprising manganese dioxide nanosheets (MNSs) and nitrogen-doped graphene aerogel (NGA), which was denoted as MNSs@NGA [55]. In this architecture, NGA acts as a conductive carbon scaffold, establishing a percolative electron-conducting pathway for MNSs while simultaneously engaging in strong interfacial heteroatomic coupling with MnO₂ via Mn-O-C/Mn-N covalent bonding. Such synergistic nanostructuring enables accelerated electron-ion co-transport, as evidenced by the Koutecky–Levich (K-L) analysis indicating a dominant 4e[−] ORR pathway. The low Tafel kinetic parameter further confirms its efficient ORR catalytic activity (Figure 5b).

Beyond augmenting the electrical conductivity of MnO₂, carbonaceous substances play a pivotal role in promoting the formation of surface oxygen vacancies (V_o) within the lattice framework of α-MnO₂. The presence of V_o optimizes electron localization, anchors high-spin Mn (III) species in oxidized states, and consequently boosts the bifunc-

tional catalytic efficiency of MnO_2 . A dual-carbon heterostructure strategy was employed, in which protonated carbon nitride ($\text{p-C}_3\text{N}_4$) was assembled with lignin-derived nitrogen/phosphorus co-doped activated carbon (NPAC). This composite was then integrated with oxygen vacancy modulation to synthesize a MnO_2 -based bifunctional oxygen electrocatalyst (MCC) (Figure 5c,d) [56]. DFT simulations demonstrated that the superior catalytic activity of MCC originates from interfacial electronic hybridization between the dual-carbon supports and MnO_2 . Specifically, the d-band center of Mn in MCC (-1.238 eV) exhibits an upward shift ($\Delta E = +0.361$ eV) relative to that in pristine MnO_2 (-1.599 eV), approaching the Fermi level. This electronic reconfiguration stabilizes the adsorption geometries of oxygen intermediates and optimizes the kinetic barriers for both the ORR and OER.

Moreover, cation doping proposes a structure–activity modulation approach for tailoring the electronic configuration of MnO_2 and optimizing its electrocatalytic performance. Zheng and colleagues fabricated a cobalt–nickel co-doped MnO_2 nanorod catalyst with a tunnel-type architecture, self-supported on conductive microfibrous carbon substrates, using a hydrothermal synthesis approach [59]. These cations (Co or Ni) partially substitute Mn ions within the $[\text{MnO}_6]$ octahedral framework through substitutional doping, thereby modulating the electronic configuration of MnO_2 by elevating the proportion of Mn^{3+} species, which subsequently induces structural deformation of the $[\text{MnO}_6]$ octahedra through the Jahn–Teller effect. Doping substantially improves the kinetics of the ORR, as demonstrated by a positive shift in the $E_{1/2}$ exceeding 20 mV and a rise in the limiting current density. The close approximation to the ideal $4e^-$ transfer pathway further corroborates this enhancement. For the OER, the doped catalysts show a reduction in overpotential at 10 mA cm^{-2} and achieve a 600% enhancement in current density relative to pristine MnO_2 at 1.76 V (vs. RHE), demonstrating synergistic bifunctional electrocatalytic activity. In contrast, a molten-salt-mediated synthesis approach was utilized to seamlessly incorporate Ru ions into the MnO_2 crystal lattice, culminating in the successful fabrication of $\text{Mn}_{0.3}\text{Ru}_{0.7}\text{O}_2$ nanosheets [60]. The solid-solution structure formed as a result facilitated the reallocation of interatomic charges between Ru and Mn atoms. Consequently, it adjusted the electronic surroundings of Mn sites by reducing their oxidation states and elevating the position of the d-band center. This electronic modulation strengthened the binding affinity of Mn sites towards oxygen-containing intermediates, which in turn expedited the kinetics of the ORR. Meanwhile, the Ru sites demonstrated elevated oxidation states and downshifted d-band centers, weakening oxygen intermediate adsorption and favoring OER kinetics. Thus, $\text{Mn}_{0.3}\text{Ru}_{0.7}\text{O}_2$ nanosheets exhibited superior bifunctional catalytic activity. Analogous to cation doping, the anchoring of metal oxides (MO_x , M = Fe, Co, Ni) on MnO_2 surfaces can also supply metal cations to modulate its electronic structure and catalytic performance. In hierarchical hybrid catalysts, MO_x species activate Mn active sites by back-donating electrons to Mn 3d orbitals, shifting their density toward lower energy levels and weakening intermediate binding. Remarkably, the anchoring of Co_3O_4 onto MnO_2/CNTs surfaces to form a distinct “core–shell” architecture demonstrated superior electrocatalytic activity compared to Fe- MnO_2/CNTs or Ni-MMnO₂/CNTs counterparts [53].

3.3. Mn_3O_4

In the spinel compound Mn_3O_4 ($\text{Mn}^{2+}\text{Mn}^{3+}_2\text{O}_4$), Mn^{2+} ions occupy tetrahedral interstices, whereas Mn^{3+} ions are stabilized within octahedral voids. This arrangement creates a densely interpenetrated cationic framework embedded within an oxygen sublattice. As a result, Mn_3O_4 exhibits unique physicochemical properties, making it an ideal candidate for O_2 -related catalytic reactions [61]. However, when compared to benchmark Pt-based catalysts, pristine Mn_3O_4 faces several limitations, including inadequate elec-

trical conductivity, high overpotentials, and issues such as dissolution or agglomeration during the catalytic process. To enhance the performance of Mn_3O_4 , similar optimization strategies used for other metal oxides have been applied, including the incorporation of conductive carbonaceous additives [62]. These materials not only improve the electronic conductivity of Mn_3O_4 -based composites but also provide various catalytic active sites. For example, the incorporation of Mn_3O_4 nanoparticles within oxygen-functionalized carbon nanotubes ($\text{Mn}_3\text{O}_4/\text{O-CNTs}$) facilitates the spatial segregation of OER and ORR active centers (Figure 6a). In this configuration, CNTs serve as nucleation sites for the growth and embedding of Mn_3O_4 nanoparticles, while simultaneously enhancing their electrical conductivity through improved connections. Additionally, the oxygen-plasma-induced functionalities on the CNTs create a high density of reactive centers that facilitate OER catalysis [63].

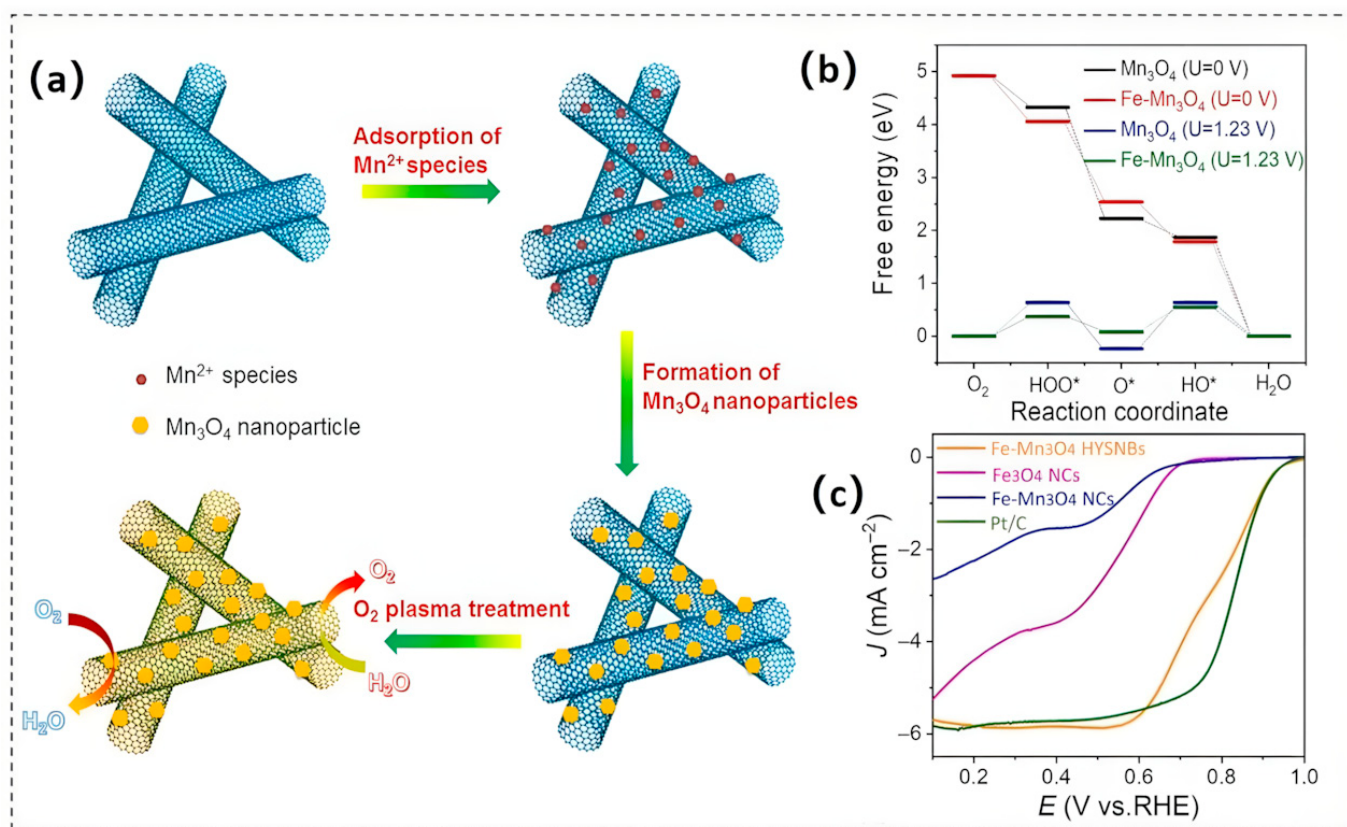


Figure 6. (a) Schematic elucidation of $\text{Mn}_3\text{O}_4/\text{O-CNTs}$ heterostructure formation. Reproduced with permission [63]. Copyright 2018 American Chemical Society. (b) A comparative analysis of the ORR free-energy pathways for Fe-doped Mn_3O_4 and pristine Mn_3O_4 is conducted at an equilibrium potential of $U = 1.23 \text{ V}$ under zero-bias conditions. (c) LSV polarization curves for $\text{Fe-Mn}_3\text{O}_4$ HYSNBs, Fe_3O_4 NCs, Fe -doped Mn_3O_4 NCs, and Pt/C benchmark. Reproduced with permission [61]. Copyright 2021 Elsevier.

The surface metal doping of Mn_3O_4 constitutes another viable approach for enhancing its electrochemical performance, which can modulate the electronic structure and binding strength of ORR intermediates, thereby enhancing the electron transfer capability towards adsorbed oxygen molecules and consequently exhibiting improved ORR performance. Doping the surface of Mn_3O_4 with metal elements is an effective strategy for enhancing its electrochemical performance. This process can adjust the electronic structure and binding strength of the ORR intermediates, which in turn improves the electron transfer capability to adsorbed oxygen molecules, resulting in better ORR performance. Metals such as

Fe [61], Co [64], and Ce [65] have been utilized to boost the electrocatalytic performance of Mn₃O₄. For instance, Li et al. [61] demonstrated the precise fabrication of hollow yolk-shell nanostructures of Fe-doped Mn₃O₄. The incorporation of Fe-induced coordinated electronic modulation within the host matrix through three synergistic mechanisms. Primarily, the integration of Fe promoted the formation of oxygen vacancies, significantly increasing the number of catalytically active sites. Additionally, this heteroatom doping caused a favorable shift in the d-band center toward the Fermi level, enhancing the overlap of orbitals with the oxygenated intermediates during electrochemical reactions. Furthermore, the modification improved the thermodynamics of adsorption and desorption for critical ORR species, as illustrated in Figure 6b. Electrochemical evaluations showed that this engineered catalyst had exceptional performance, achieving an onset potential (E_{onset}) of 1.02 V and a half-wave potential ($E_{1/2}$) at 0.78 V while maintaining exceptional stability over prolonged operation cycles (Figure 6c).

Furthermore, the construction of heterostructure interfaces has been recognized as a crucial method for enhancing the catalytic performance of Mn₃O₄-based materials. This approach facilitates interactions in the electronic structures of different materials, which facilitates charge redistribution and optimizes the activity of catalytic sites. A Co₃O₄/Mn₃O₄/N-rGO hybrid catalyst with heterointerfaces was synthesized by Huang's research group [66]. DFT calculations revealed that the formation of these heterointerfaces promotes a reconfiguration of charge density. As a result, the highly conductive Co₃O₄ phase promotes directional electron transfer to the semimetallic Mn₃O₄, resulting in exceptional electrical conductivity for the Co₃O₄/Mn₃O₄/N-rGO hybrid catalyst. Additionally, engineering these heterointerfaces increases both the density of catalytic active centers and the electrolyte-accessible surface area. This optimization enhances the utilization efficiency of the active sites and synergistically boosts the catalytic activity of Mn₃O₄.

3.4. Mn₂O₃

A plethora of research has demonstrated that Mn₂O₃, owing to its distinctive electronic configuration and facile synthesis, exhibits remarkable efficacy as a bifunctional catalyst for oxygen electrocatalytic reactions [67]. Nevertheless, the practical applications of pure Mn₂O₃ are hindered by its suboptimal electrical conductivity, inadequate active site density, and compromised operational stability. Among various strategies, morphological engineering stands out as a cornerstone approach to enhance the catalytic efficacy and durability of Mn₂O₃. Specific morphologies, including nanosheets [68], spheres [69], hollow structures [70], and yolk-shell architectures [71], offer high specific surface areas and porosity, facilitating mass/charge transport and thereby promoting ORR/OER activities. As research progresses, morphological modulation is often combined with other strategies to further elevate the catalytic performance of Mn₂O₃. As a case in point, the research group led by Ma devised a self-assembly–oxidation coupled synthesis approach to fabricate a Mn₂O₃/RuO₂ heterojunction nanocomposite encapsulated within nitrogen-doped porous carbon microspheres (Mn₂O₃/RuO₂/NCS) (Figure 7a) [72]. This catalyst features a hierarchical yolk-shell architecture with tunable internal cavities and porous interfaces, enhancing active site–electrolyte contact and mass-transfer kinetics. The Mn₂O₃/RuO₂ heterointerface facilitates interfacial electron redistribution, modulates metal–oxygen coordination, and optimizes OER/ORR intermediate adsorption, collectively boosting the bifunctional catalytic activity of Mn₂O₃ (Figure 7b). Rechargeable ZABs employing the Mn₂O₃/RuO₂/NCS catalyst delivers 153.5 mW cm⁻² peak power density, 59.35% round-trip efficiency, and 850 h cycling stability. In contrast to the aforementioned study, Shao and colleagues achieved enhanced catalytic performance by bridging NiO and Mn₂O₃ with carbon dots to form a heterostructure [73].

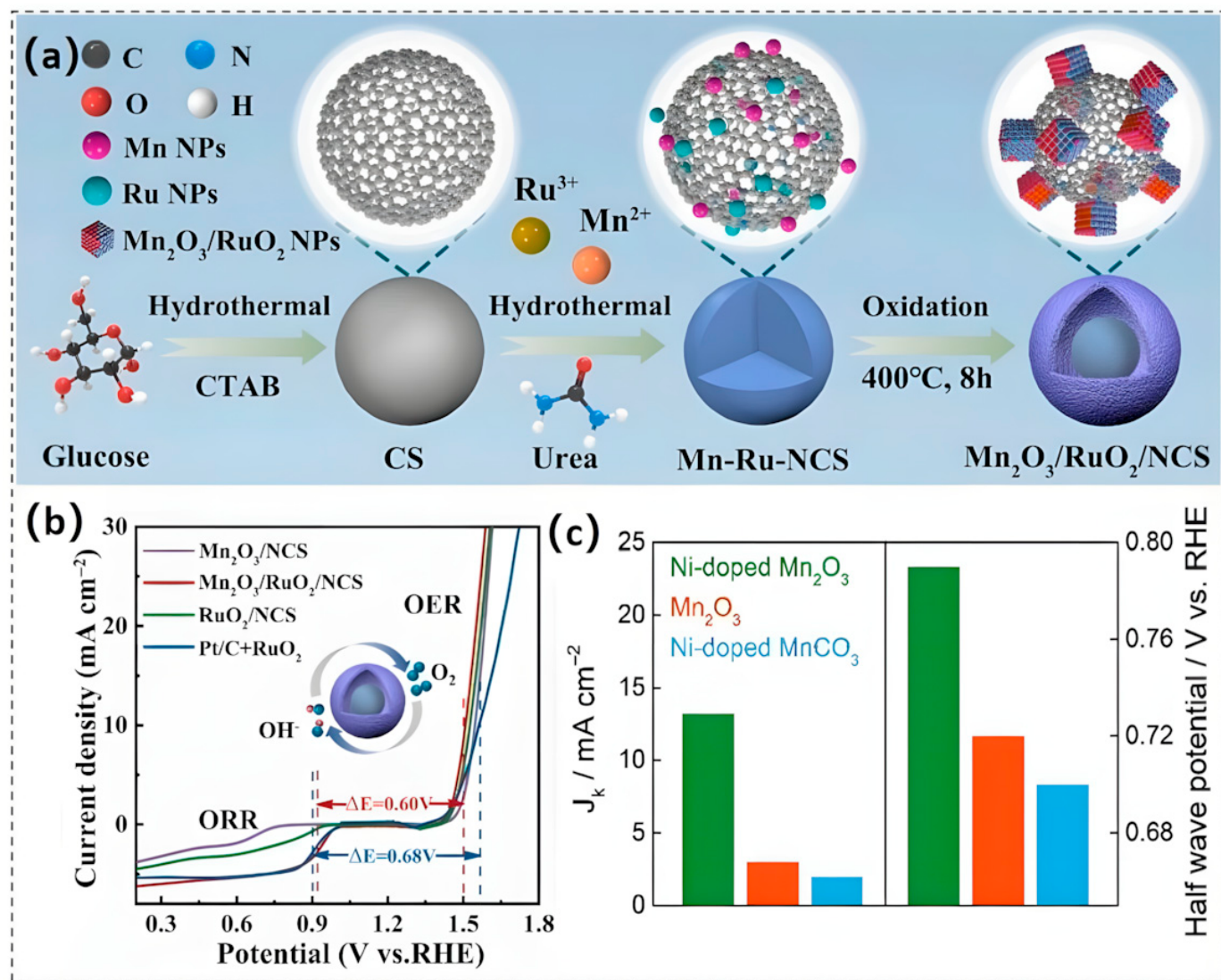


Figure 7. (a) The preparation methodology for $\text{Mn}_2\text{O}_3/\text{RuO}_2/\text{NCS}$. (b) Bifunctional LSV profiles for ORR and OER. Reproduced with permission [72]. Copyright 2024 Elsevier. (c) Contrastive analysis of the kinetic current density measured at 0.75 V versus RHE and the half-wave potential among Ni-doped MnCO_3 , pristine Mn_2O_3 , and Ni-doped Mn_2O_3 . Reproduced with permission [74]. Copyright 2021 Elsevier.

Similarly to other manganese oxides introduced above, heteroatom doping has also been systematically implemented to tailor the electronic configuration of Mn_2O_3 by introducing surface defect engineering, which synergistically augments its intrinsic electrical conductivity and generates oxygen-vacancy-dominated active centers, ultimately elevating the electrocatalytic efficiency. Kim et al. [74] successfully synthesized Ni-doped Mn_2O_3 microspheres through a co-precipitation and heat treatment process. Compared with undoped Mn_2O_3 , the Ni-doped Mn_2O_3 exhibited a higher electrochemically active surface area and superior ORR electrocatalytic activity. The experimental results demonstrate that Ni incorporation effectively optimizes electron transport pathways through increased surface exposure, generates additional electrocatalytic active centers, and facilitates oxygen species diffusion (Figure 7c). When implemented in rechargeable ZABs, the Ni-Mn₂O₃ composite catalyst delivers superior electrochemical performance with a recorded specific capacity of 813.5 mAh g^{-1} (Zn) and gravimetric energy density of 1038.2 mAh g^{-1} (Zn), representing an enhancement over conventional Pt/C counterparts.

Table 3. Performance summary of Mn-based oxides as bifunctional electrocatalysts performance in rechargeable ZABs.

Electrocatalysts	OER E_{10} [V]	ORR $E_{1/2}$ [V]	OCV [V]	Performance (ZABs)			Ref.
				Specific Capacity [mAh g ⁻¹]	Peak Power Density [mW cm ⁻²]	Stability	
Co-Mn ₃ O ₄ /G	1.505	0.866	1.415	-	115.24	945 cycles@10 mA cm ⁻²	[64]
α -MnO ₂ Nanowires	1.625	0.83	1.51	717	166	40 h@100 mA cm ⁻²	[75]
Mn _{0.3} Ru _{0.7} O ₂ nanosheets	1.44	0.85	1.52	821	154	200 h	[60]
MC@NC	1.59	0.82	1.43	950	153	300 h@4 mA cm ⁻²	[46]
Co@C,MnO-NAC	1.55	0.83	1.46	-	58	37 h@5 mA cm ⁻²	[45]
Ni MnO/CNF	1.58	0.83	1.563	-	138.6	350 cycles @10 mA cm ⁻²	[50]
Co-MnO ₂ /CNTs	1.65	0.872	1.578	-	342.5	129 h	[53]
Co ₃ O ₄ /Mn ₃ O ₄ (2:1)/N-rGO	1.59	0.86	1.54	-	194.6	2000 cycles	[66]
Co@Co ₄ N/MnO-NC	1.62	0.81	1.47	762	200.5	2800 cycles@10 mA cm ⁻²	[76]
Mn _x O _y /C (ZMC)	-	0.763	1.443	-	140	-	[77]
MnO (II)	-	0.895	-	-	63.2	>35 h@40 mA cm ⁻²	[78]
FG-MnO _x	-	-	-	-	170	100 h	[79]

4. Manganate

Compared to pure manganese oxides, manganates demonstrate significant potential for high-efficiency catalysis in rechargeable ZABs. This is achieved through the synergistic charge transfer between the Mn³⁺ and Mn⁴⁺ oxidation states, the high density of active sites provided by their three-dimensional framework structures, and the precise modulation of surface electronic states via defect engineering. Among these materials, manganese-based perovskites and spinels are the two most extensively studied families. The related electrochemical performances are listed in Table 4. The following sections will detail their structural characteristics and modification strategies separately.

4.1. MMnO₃

ABO₃-structured perovskite oxides have attracted significant scientific interest due to their flexible crystalline frameworks, abundant defect sites, and tunable electronic states [80–82]. Among them, LaMnO₃ is a notable perovskite that exhibits remarkable electrocatalytic activity attributed to the presence of mixed manganese valence states (Mn³⁺/Mn⁴⁺) [83]. Notably, recent research advancements in the field of nanostructured perovskite electrocatalysts, particularly the innovative synthesis methods tailored for LaMnO₃-based materials, have further enhanced their electrocatalytic performance [84,85]. When used as a cathode material in rechargeable ZABs, LaMnO_{3+δ} shows a near-ideal OCV of 1.43 V, which is 97.3% of the benchmark OCV of 1.47 V achieved by commercial Pt/C catalysts. Under operational conditions with a current density of 200 mA cm⁻², the ZABs produce a power density of 198.6 mW cm⁻², only 2.1% lower than that of the battery using Pt/C catalysts at the same catalyst loading. This finding confirms the effectiveness and practical viability of LaMnO_{3+δ} as a cathode catalyst in rechargeable ZABs [86].

However, LaMnO₃ suffers from inherent issues such as poor electrical conductivity, inadequate chemical stability, and a need for further enhancement in catalytic activity. It has been demonstrated that employing an A-site deficiency strategy (e.g., introducing Sr [87], Ce [88]) combined with B-site doping techniques (e.g., incorporating transition metals such as Co [89], Ni [90], Fe [83]) in LaMnO₃ can significantly improve its catalytic performance. Specifically, A-site deficiency enhances catalytic activity by inducing Mn⁴⁺ species enrichment and the formation of surface V_o [91]. Utilizing the sol–gel technique, a series of La_{1-x}Ce_xMnO₃ perovskite-type oxides were successfully synthesized [88]. The research revealed that when a portion of La³⁺ in LaMnO₃ was substituted with Ce⁴⁺, the relative surface abundance of Mn⁴⁺ increased. Specifically, it rose from 45.4% in LaMnO₃ (LMO) to 49.9% in the Ce-doped sample with a doping level of 0.10 (LCMO-0.10). Simultaneously, the surface coverage of adsorbed oxygen also saw an uptick, going from 41.7% in LMO to 47.2% in LCMO-0.10. These alterations promote the exchange process of O₂²⁻/OH⁻, which subsequently contributes to the improvement of ORR performance. Concurrently, B-site doping optimizes catalytic efficacy via valence state modulation, active site density augmentation, and oxygen transport activation energy reduction [92]. A bi-functional La(Ni_{0.1})MnO₃ perovskite modified with N-doped carbon to enhance its activity was developed through a B-site doping strategy (Figure 8a) [90]. The La(Ni_{0.1})MnO₃@NC composite demonstrates markedly enhanced ORR activity relative to pristine LaMnO₃, achieving a diffusion-limiting current density (J_L) of 5.8 mA cm⁻² alongside an E_{onset} and E_{1/2} of 0.91 V and 0.77 V, respectively. The remarkable performance observed can primarily be ascribed to the synergistic interactions facilitated by the porous architecture, which provides a large surface area, along with the moderate coupling of the preserved active species within the [NiO₆] and [MnO₆] octahedral units. Moreover, the heteroatom-doped carbon material, serving as a highly conductive catalyst support, plays an indispensable role in enhancing the electron and ion transport capabilities as well as the catalytic activity [93].

Furthermore, untreated manganese-based perovskites face inherent limitations, such as cation segregation and a reduced specific surface area. These issues collectively hinder the efficiency of electrochemical utilization [94]. Surface modification presents a promising solution to address these challenges. By selectively dissolving the segregated cations on the surface of the perovskite, this approach increases the available specific surface area and promotes the formation of V_o. These two effects work together to significantly enhance the material's catalytic and electrochemical properties. V_o is well-known for its crucial role in influencing reaction kinetics and altering reaction mechanisms [95,96]. Li and colleagues adopted a surface pre-restructuring protocol to synthesize Fe-doped La_{0.7}Sr_{0.3}MnO₃ nanoparticles (LSM/Fe-1.5) [97]. The optimized catalyst demonstrated improvements of 1.8 times in the ORR activity and 4.9 times in the OER activity (Figure 8b,c). This enhancement in ORR is attributed to the dissolution of A-site cations induced by Fe³⁺, which modifies the Mn³⁺/Mn⁴⁺ redox couple through electronic structure engineering. This process raises the concentration of V_o and facilitates bidentate O₂ adsorption. The charge reorganization associated with V_o effectively reduces H₂O₂ generation by encouraging a four-electron reduction pathway, thus increasing the number of electrons transferred. Additionally, the deliberate adjustment of the B-site electronic configuration weakens the binding affinity of reaction intermediates, accelerating the ORR kinetics by lowering activation energy barriers. In terms of OER, the increased catalytic activity arises from the synergistic relationship between the enhanced adsorption capacity of Fe on the perovskite surface and the cooperative electronic interactions between Fe³⁺ dopants and surface V_o species (Figure 8d).

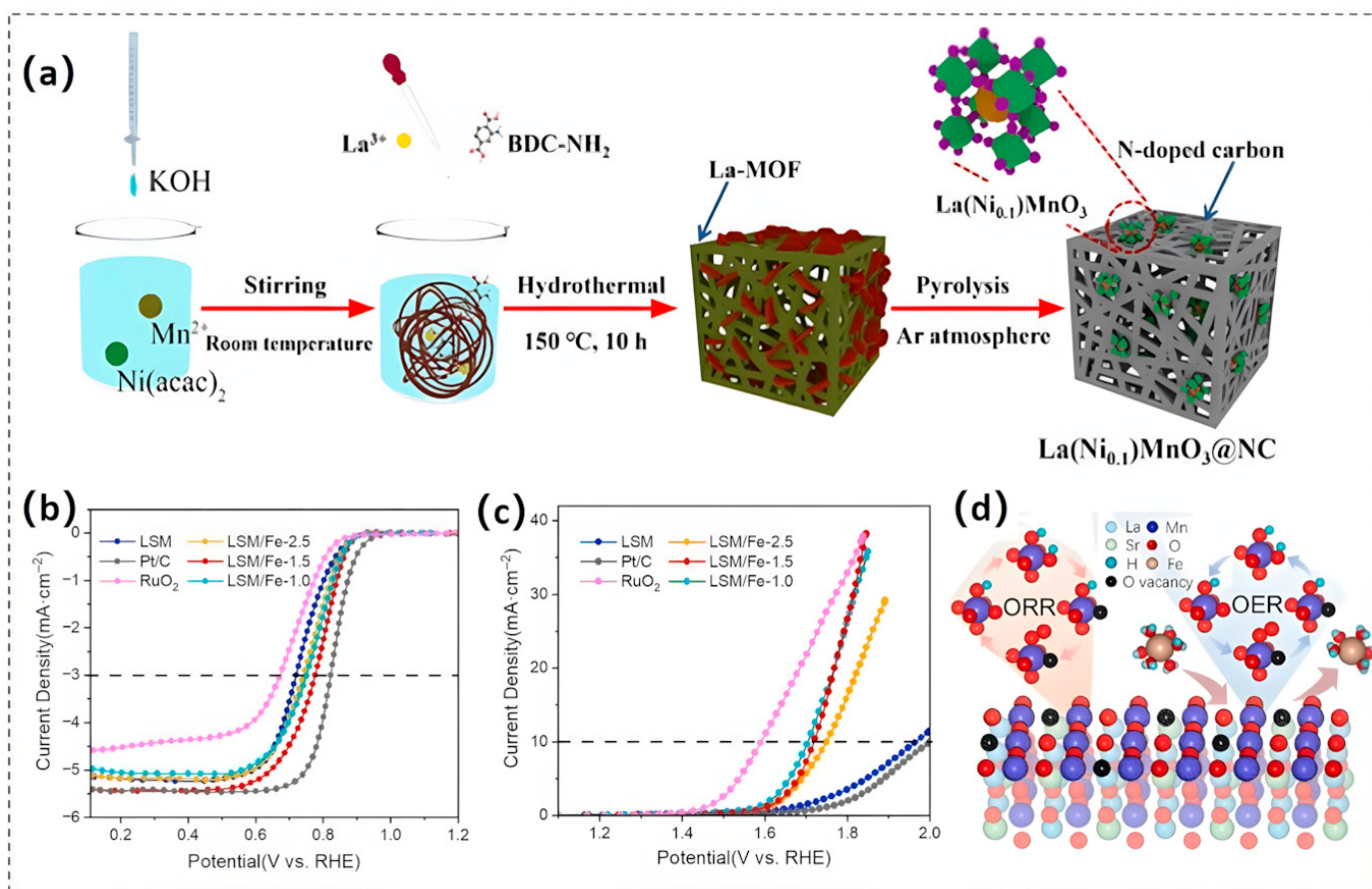


Figure 8. (a) Schematic depiction of the synthesis procedure for the $\text{La}(\text{Ni}_{0.1})\text{MnO}_3@\text{NC}$ catalyst. Reproduced with permission [90]. Copyright 2023 American Chemical Society. (b) ORR and (c) OER polarization curves of LSM, Fe-doped LSM/Fe-x series catalysts, commercial Pt/C, and RuO₂ under O_2 -saturated 0.1 M KOH electrolyte (scan rate: $5 \text{ mV}\cdot\text{s}^{-1}$; rotation rate: 1600 rpm for ORR). (d) Catalytic mechanism underlying the ORR and OER. Reproduced with permission [97]. Copyright 2023 Elsevier.

In addition to designing novel manganese-based perovskites free of noble metals, another viable approach entails coupling non-noble metals with low-loading, yet highly efficient noble-metal components to optimize atomic utilization and catalytic performance. This strategy exploits the electronic structure modulation of electrocatalysts via intermetallic synergistic effects, thereby dictating their bifunctional electrocatalytic performance. As an illustration, Dai and his group [98] showed excellent bifunctional catalytic activity by combining ultrafine RuO_x with $\text{La}_{0.8}\text{Sr}_{0.2}\text{Mn}_{0.5}\text{Co}_{0.5}\text{O}_3$ perovskite.

4.2. MMn_2O_4 and MnM_2O_4

Spinel oxides (AB_2O_4) are characterized by a dual-site framework comprising tetrahedrally coordinated A-sites (denoted as M_{Td}) and octahedrally coordinated B-sites (denoted as M_{Oh}), which collectively define their structural anisotropy and catalytic functionality. This distinctive structural topology allows identical or distinct transition metal elements to flexibly occupy both M_{Td} and M_{Oh} positions, thereby endowing spinel oxides with exceptional structural adaptability and tunability [99]. Based on the Mn occupancy within the spinel lattice, manganese-based spinels can be categorically classified into two primary types: (1) the MMn_2O_4 -type ($\text{M} = \text{Co, Ni, Zn, etc.}$), where Mn serves as the central ion occupying M_{Oh} sites, and (2) the MnM_2O_4 -type, where Mn resides in M_{Td} positions. Among these, Co/Mn-based spinel oxides have demonstrated significant potential as oxygen elec-

trocatalysts attributed to their tunable valence configurations and distinct crystal structures. However, their practical application remains constrained by critical limitations, including suboptimal bifunctional catalytic activity, inadequate durability, and inefficient oxygen transport kinetics at the three-phase interface.

The integration of spinel oxides with carbon nanostructures, particularly heteroatom-doped (e.g., N, S) carbonaceous architectures, represents a highly effective strategy for enhancing their performance. Electrospinning technology provides an elegant implementation of this approach, enabling intimate mixing of N-doped carbon nanofibers (N-CNFs) with metal-active phases to successfully synthesize Co_2MnO_4 spinel nanoparticles anchored on N-CNF. The coexistence of redox-active couples ($\text{Mn}^{4+}/\text{Mn}^{3+}$ and $\text{Co}^{3+}/\text{Co}^{2+}$) and surface nitrogen moieties (graphitic and pyridinic N) within the hybrid catalyst endows it with bifunctional catalytic excellence [100]. In addition to the aforementioned methods, atomic-scale surface engineering strategies, such as introducing defects and regulating the distribution of surface elements, are also widely adopted to optimize the catalytic efficacy and functionality of the materials. Taking the preparation of Co_2MnO_4 nanosheets (denoted as C₂M) via a coprecipitation method combined with acid treatment as an example, the resulting nanosheets possess a Mn-enriched surface and a large number of twin-boundary defects. Research findings indicate that the Mn-enriched surface facilitates the bridged adsorption of O_2 with lower energy, thereby promoting the four-electron transfer mechanism in the ORR (Figure 9a). Simultaneously, the cation occupation at multivalent sites facilitates Mn/Co-O orbital hybridization, leading to the formation of impurity states within the bandgap, which accelerates charge transfer (Figure 9b). Moreover, the acid treatment process effectively mitigates Mn leaching during the catalytic reaction, further enhancing the durability of C₂M in ORR [101].

In addition to introducing defects via optimized synthesis methods to enhance catalytic activity and durability, metal doping represents another widely adopted modification strategy. In manganese-based spinels, the A_{Td} and B_{Oh} sites are uniquely connected through corner-sharing and edge-sharing oxygen bridges, rendering the electronic state of B_{Oh} highly susceptible to the electronic influence of ions occupying either the A_{Td} sites or neighboring B_{Oh} positions. Consequently, the incorporation of a third metal ion, such as Cr³⁺ [102] or Ni²⁺ [103,104] enables the effective modulation of the B_{Oh} electronic structure, thereby optimizing catalytic performance. Liu's research team designed a series of Cr³⁺-doped spinel oxides with the crystal structure depicted in Figure 9c [102]. Their analysis demonstrated that in $\text{CoMn}_{2-x}\text{Cr}_x\text{O}_4$ ($x = 0\text{--}2$), the e_{9g} orbital occupancy of octahedral transition metal cations (TM_{Oh}) diminish from 2 to 0 with increasing Cr substitution. This reduction facilitates Cr³⁺-mediated orbital hybridization between transition metal 3d and oxygen 2p orbitals through interactions with vacant e_{9g} states. This orbital coupling reconfigures the electronic configuration of the catalyst, enhancing its electrical conductivity and subsequently boosting electrocatalytic performance (Figure 9d).

Besides the aforementioned Co/Mn-based spinel oxides, other manganese-containing spinels, such as ZnMn₂O₄ nanospheres [105] and NiMn₂O₄ nanosheets [106], have also been reported. José Béjar et al. [106] synthesized small-sized NiMn₂O₄ spinels using an electrodeposition approach, resulting in a three-dimensional (3D) porous architecture composed of interconnected nanosheets. The hierarchical architecture of this material facilitates the exposure of a large number of active sites and, at the same time, enhances the mass/charge transfer kinetics through an optimized network for ion/electron diffusion. Critically, the surface defect ensemble (including V_o, dislocations, and lattice strain) acts as a catalytic performance enhancer. In rechargeable ZAB tests, the NiMn₂O₄ electrode exhibits a peak power density (74 mW cm⁻²) similar to what the benchmark catalyst can achieve, coupled with exceptional cycling durability over extended charge-discharge cycles.

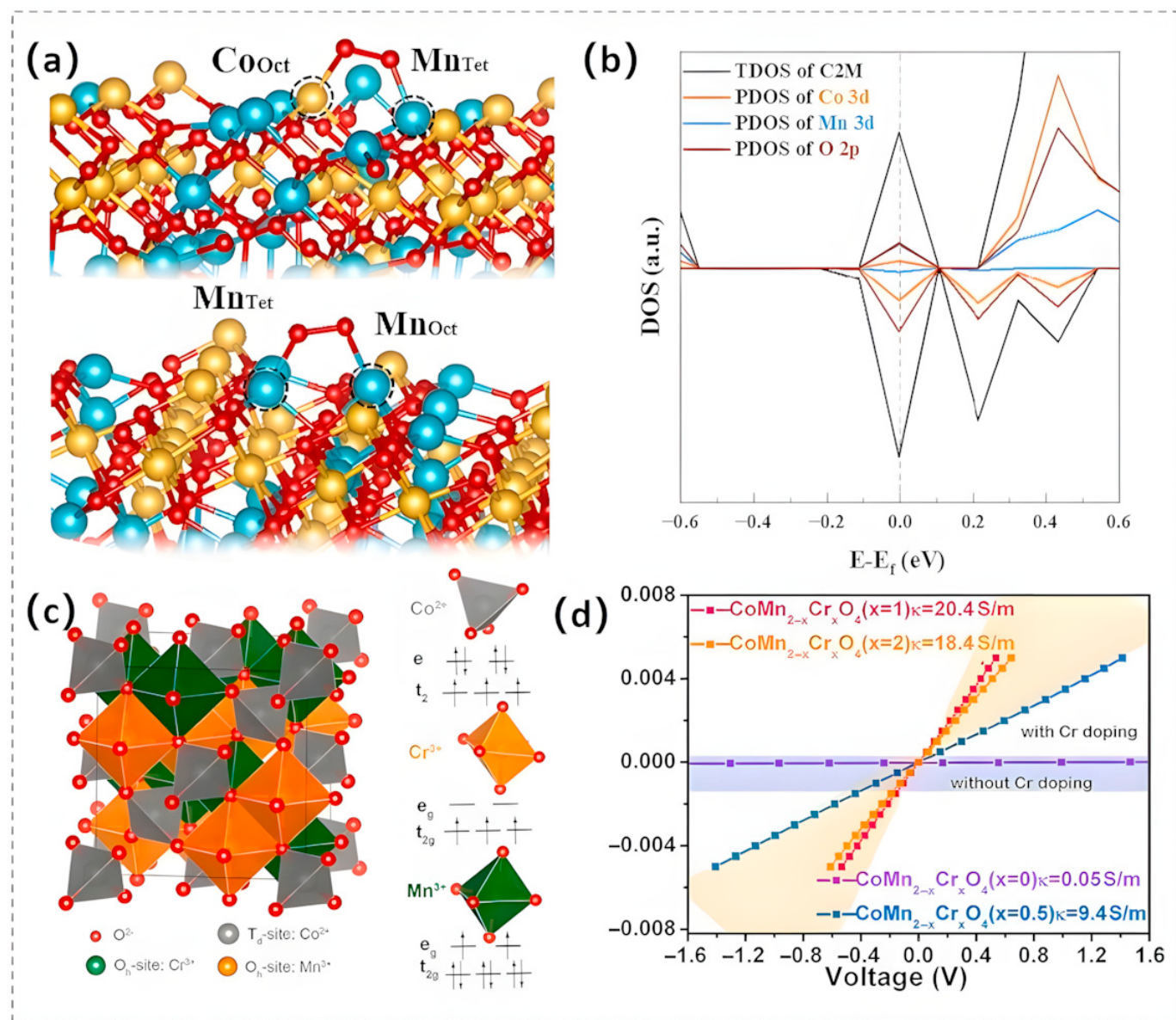


Figure 9. (a) Bridge adsorption configurations of O_2 on Co_{Oct}/Mn_{Tet} and Mn_{Oct}/Mn_{Tet} sites in the C_2M catalyst. (b) An extended depiction of the PDOS for C_2M in the vicinity of the Fermi level. Reproduced with permission [101]. Copyright 2023 Elsevier. (c) A polyhedral structural representation of spinel oxides, accompanied by a schematic depicting the d-orbital configurations of Co^{2+} , Mn^{3+} , and Cr^{3+} . (d) The I-U curves of $CoMn_{2-x}Cr_xO_4$ ($x = 0–2$). Reproduced with permission [102]. Copyright 2020 Elsevier.

Table 4. Summary of performance of manganates as bifunctional electrocatalysts in ZABs.

Electrocatalysts	ORR			Performance (ZABs)			Ref.
	OER E_{10} [V]	$E_{1/2}$ [V]	OCV [V]	Specific Capacity [mAh g ⁻¹]	Peak Power Density [mW cm ⁻²]	Stability	
$CoMn_{2-x}Cr_xO_4/N-rGO$	1.52	0.82	1.37	806.89	140.26	43 h@10 mA cm ⁻²	[102]
$CoMn_{1.5}Ni_{0.5}O_4$	1.643	0.780	1.6	-	147.4 (aqueous state) 85.8 (solid state)	-	[103]

Table 4. *Cont.*

Electrocatalysts	ORR			Performance (ZABs)			Ref.
	OER E ₁₀ [V]	E _{1/2} [V]	OCV [V]	Specific Capacity [mAh g ⁻¹]	Peak Power Density [mW cm ⁻²]	Stability	
Co _{0.5} Ni _{0.5} Mn ₂ O ₄	1.78	0.65	1.36	808.9	49	10 h@2 mA cm ⁻²	[104]
ZnMn ₂ O ₄	1.813	0.75	-	-	-	40 cycles@10 mA cm ⁻²	[105]
NiMn ₂ O ₄	1.85	0.74	1.30	-	72	300 cycles@10 mA cm ⁻²	[106]
Ball-milled Ni-Co-Mn oxides	1.597	-	1.45	-	85.42	100 h@10 mA cm ⁻²	[107]
Optimized Co-Mn spinel cathode	1.587	0.898	-	717.7	-	2000 cycles@10 mA cm ⁻²	[108]
Co ₂ MnO ₄ /NCNTs	1.593	0.76	1.48	827	74.63	300 cycles@5 mA cm ⁻²	[109]
ZnMn _{1.4} Co _{0.6} O ₄ /NCNTs	-	0.77	1.48	848	93	280 h@5 mA cm ⁻²	[110]
MnCo ₂ O ₄ 3DOM	-	0.94	1.49	1004	98.7	-	[111]
CoMn ₂ O ₄ 3DOM	-	0.96	1.42	1440	101.6	-	[111]

5. Other Manganese-Based Compounds

5.1. Mn-LDHs

Manganese-based layered double hydroxides (Mn-LDHs) have recently garnered significant interest as a key research topic within the field of electrochemical technologies, owing to their unique two-dimensional structure, excellent ion-exchange capacity, abundant surface hydroxyl groups, and numerous active sites [112,113]. Among them, NiMn-LDH and CoMn-LDH exhibit outstanding activity in OER catalysis. However, the inherent low electrical conductivity of LDHs and the deterioration of active sites due to material stacking severely limit their practical applications. Furthermore, their sluggish ORR kinetics also restrict their widespread application in secondary rechargeable ZABs.

To address the insufficient electrical conductivity of LDHs, incorporating them into high-conductivity frameworks, such as carbon nanotubes, graphene oxide, and conductive metals, is a viable strategy for improving their electrochemical performance. For example, in the hybrid system composed of conductive silver nanowires (Ag NWs) integrated with NiMn-LDHs, the incorporation of Ag NWs not only significantly enhances the electronic conductivity of the composite but also alleviates the agglomeration of LDH nanosheets, thereby exposing a highly accessible electrochemical surface area. This expansion of the surface area, which is closely related to the density of active sites, significantly improves both the catalytic efficiency and durability of the hybrid material, as demonstrated by experimental results [114]. Similarly, the combination of highly conductive CNTs with CoMn-LDH nanosheets can also improve the electron transport properties of Mn-LDHs (Figure 10a), resulting in an increase in their electrocatalytic activity. The resulting hybrid materials demonstrate a notably reduced overpotential, a substantially decreased Tafel slope, and exceptional electrochemical stability [115].

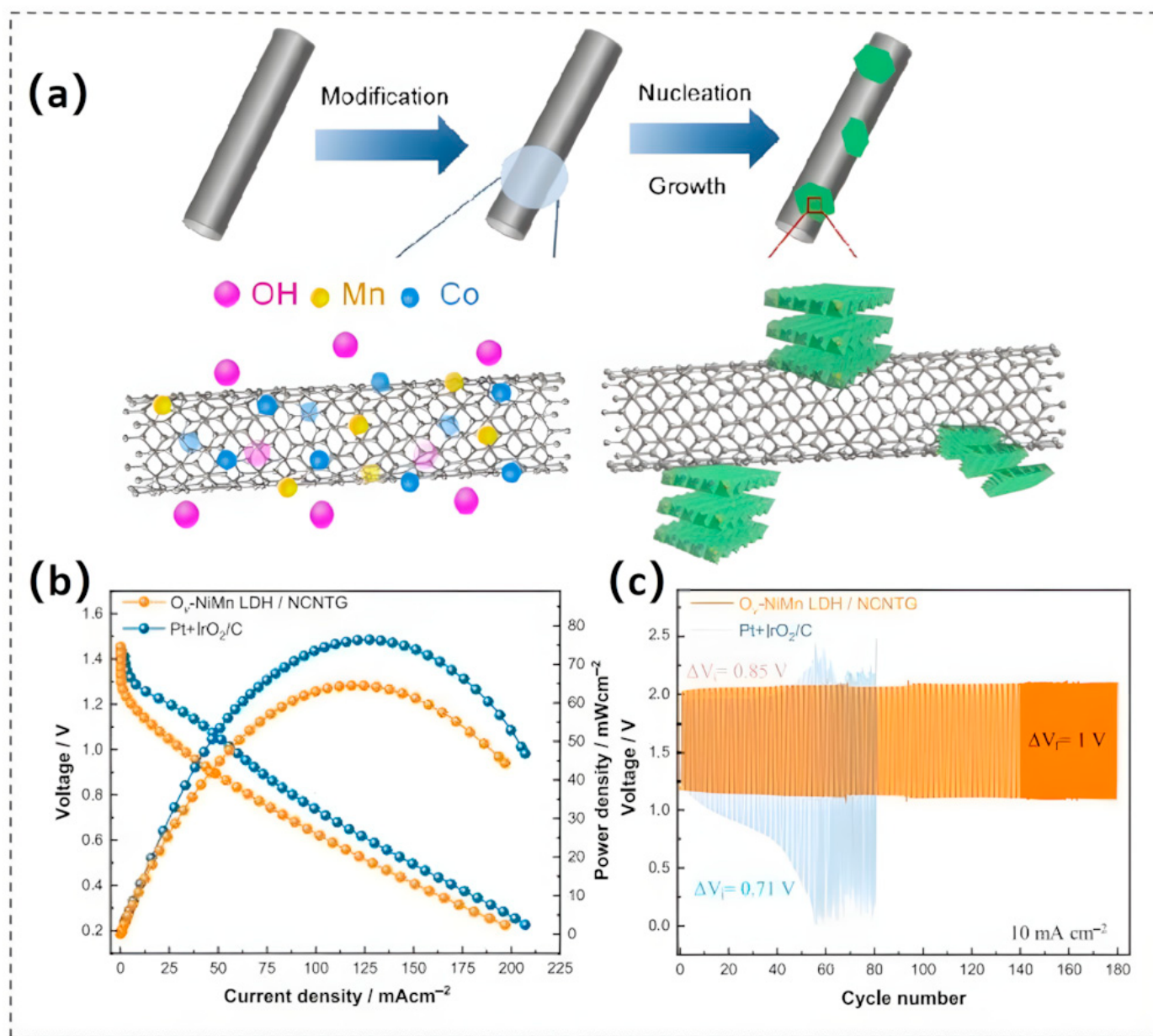


Figure 10. (a) Illustrative process for the synthesis of CoMn-LDH/CNT nanocomposites. Reproduced with permission [115]. Copyright 2016 Wiley-VCH GmbH. (b) Polarization curves and power density profiles for V_o-NiMn LDH/NCNTG versus the benchmark Pt/C + IrO₂/C hybrid catalyst. (c) Cyclic charge-discharge voltage profiles. Reproduced with permission [7]. Copyright 2024 Elsevier.

Furthermore, structural engineering strategies are a pivotal approach for improving the catalytic efficiency and long-term stability of Mn-LDHs. By carefully designing hollow spherical structures composed of ultrathin CoMn double hydroxide nanosheets, highly efficient multifunctional catalytic performance can be attained [116]. This unique structure not only significantly increases the density of accessible active sites exposed to the electrolyte but also promotes rapid gas product release due to its hollow characteristics, effectively preventing the blockage of active sites caused by product accumulation during catalysis, thus exhibiting excellent catalytic activity and stability.

Moreover, to address the limitation of bifunctional electrocatalytic performance in Mn-LDHs, the synergistic application of surface defect engineering and interface engineering has emerged as an effective strategy for precisely modulating their electronic structures and active sites. Oscar et al. [7] successfully introduced V_o onto the surface of NiMn LDHs

via a chemical reduction method. This approach induced the generation of mid-gap defect states, thereby refining the electronic energy landscape and expediting electron migration kinetics during the ORR. Concurrently, the introduction of V_o resulted in the exposure of additional metal cations (particularly Mn sites) on the LDH surface. These cations served as highly efficient catalytic active centers, effectively lowering the adsorption energies of oxygenated species and significantly accelerating the kinetic process of OER. Notably, the incorporation of nitrogen dopants not only introduced supplementary active sites but also profoundly altered the local electronic environment, thus contributing significantly to the enhanced performance. In subsequent rechargeable ZAB tests, the material with introduced V_o exhibited an OCV (1.47 V) comparable with the benchmark catalyst, while demonstrating exceptional cyclic stability and long-life characteristics (Figure 10b,c).

5.2. Manganese Sulfide

Nanostructured manganese sulfides have emerged as pivotal materials in electrochemical research, attributed to their unique electronic structures, high conductivity, and facile synthesis processes [117–119]. Among them, heterogeneous manganese sulfide structures exhibit tremendous potential due to their high-density active site ensembles at interfacial regions, including edges, corners, defects, and vacancies [120]. Specifically, Chen's group successfully constructed a triphasic Co/Co₉S₈/MnS heterojunction interface by introducing the MnS phase into the Co/Co₉S₈ heterostructure [121]. The interface not only expedites the kinetics of electron transport but also triggers a modulation of the electronic landscape through interfacial charge redistribution and the hybridization of frontier orbitals. Furthermore, the abundant heterojunction interfaces introduce additional active sites that promote intimate electrolyte–intermediate contact, thereby synergistically enhancing the intrinsic activities of oxygen electrocatalysis reaction. Similarly, the fabrication of a V₂O₃/MnS heterostructure hybrid electrode for OER/ORR was reported [122]. Interface engineering strategies effectively optimized the heterojunction's capability to regulate adsorption free energy of essential intermediates across dual reaction pathways, leading to accelerated catalytic kinetics. In practical evaluations employing liquid rechargeable ZAB configurations, the V₂O₃/MnS/CC cathode demonstrated exceptional energy conversion characteristics, delivering a peak power density of 118 mW cm⁻² alongside a substantial capacity retention of 808 mAh gZn⁻¹.

5.3. Manganese Phosphide and Manganese Nitride

The unique electronic configuration of P enables it to sequester electrons from neighboring metal atoms, thereby modulating the charge density at catalytic sites and optimizing the binding affinity for reaction intermediates/products. Consequently, research on manganese phosphides as catalysts for the OER has garnered increasing attention [123]. For example, the research team led by Zhang employed a one-pot *in situ* doping-phosphorization strategy to synthesize an N,P co-doped carbon-based electrocatalyst (MnSA-MnP-980 °C) incorporating MnP nanoparticles (NPs) and single-atom Mn sites [19]. The MnP nanoparticles, which serve as a pivotal component, enhance the catalyst's adsorptive capacity for reaction intermediates. Meanwhile, the cooperative coupling between monodispersed Mn atomic centers and MnP nanocrystalline domains induced strategic electronic configuration engineering of manganese species, preferentially maintaining their low oxidation states while minimizing activation barriers for oxygen reduction processes. Systematic electrochemical characterization demonstrated superior catalytic performance of the MnSA-MnP-980 °C composite in alkaline environments, attaining the E_{1/2} of 0.88 V, while concurrently demonstrating sustained operational durability and methanol resistance.

In recent years, substantial research attention has been directed toward transition metal nitrides within the realm of metal electrocatalysts, owing to their distinctive physicochemical and electronic attributes [124]. The integration of nitrogen into transition metal lattices leads to an elevation of the d-band electron density and a concomitant narrowing of the d-band width, thereby yielding an electronic structure and cross-Fermi-level density of states (DOS) akin to those of noble metals. Davari et al. [125] successfully synthesized manganese nitride catalysts containing Mn_4N and $Mn_6N_{2.58}$ phases by high-temperature nitridation of manganese powder, and evaluated their bifunctional electrocatalytic performance in rechargeable ZABs for the first time. Notably, the 10h-annealed sample demonstrated the most favorable E_{onset} for the ORR and superior durability compared to all tested electrocatalysts. When integrated into rechargeable ZABs, this catalyst achieved a 52.7% energy conversion efficiency after 14 h of uninterrupted charge–discharge cycling at a current density of 7.5 mA cm^{-2} . This result clearly highlights the catalyst’s promising potential for practical applications in energy storage.

6. Summary and Outlook

In the field of renewable energy conversion and storage, rechargeable ZABs demonstrate significant application potential due to their high theoretical energy density, cost-effectiveness, and environmental friendliness. As a critical component of the air cathode in rechargeable ZABs, manganese-based electrocatalysts are regarded as highly promising bifunctional oxygen electrocatalysts owing to their tunable oxidation states, flexible crystal structures, and environmental benignity. This paper systematically reviews the latest research progress on manganese-based electrocatalysts in rechargeable ZABs, particularly focusing on the catalytic performance of Mn–N–C electrocatalysts, manganese oxides, manganates, and other manganese-based compounds in the ORR and OER. It also provides an in-depth analysis of the challenges and opportunities they face. Despite the remarkable performance of manganese-based electrocatalysts in rechargeable ZABs, they still suffer from inherent drawbacks such as poor electrical conductivity, unstable catalytic activity, structural collapse, and low oxygen evolution reaction efficiency. To address these shortcomings, researchers have proposed various improvement strategies, including morphological regulation, structural engineering, carbon hybridization, heterointerface construction, heteroatom doping, and defect engineering in Table 5. These strategies significantly enhance the catalytic activity and stability of manganese-based electrocatalysts by optimizing their microstructures, electronic structures, and surface properties.

To further promote the application of manganese-based electrocatalysts in rechargeable ZABs, future research should focus on the following aspects:

- (1) Elucidating Catalytic Mechanisms: By combining experimental exploration with theoretical simulations, a deep understanding of the specific catalytic roles and synergistic effects of each constituent element in manganese-based catalysts during ORR and OER should be achieved, providing a theoretical basis for the rational design of catalysts.
- (2) Optimizing Catalyst Design: Based on a comprehensive understanding of reaction pathways, surface/interface behaviors, and deactivation factors, systematic and rational design of manganese-based electrocatalysts should be conducted, including optimization of their structures, compositions, and morphologies, to improve their catalytic activity and stability.
- (3) Developing In Situ Characterization Techniques: Utilizing in situ Raman, infrared spectroscopy (IR), X-ray diffraction (XRD), X-ray photoelectron spectroscopy (XPS), and other in situ characterization techniques, the real-time tracking of reaction pathways and a comprehensive understanding of reaction mechanisms should be achieved, providing direct evidence for catalyst improvement.

- (4) Establishing Standard Evaluation Systems: For the commercialization of rechargeable ZABs, a series of standard evaluation criteria for catalytic/battery performance testing should be established to unify evaluation standards, promote the dissemination and application of ZAB technology, and drive the development of the entire industry [126].

Table 5. Comparative analysis of optimization strategies: key advantages and limitations.

Optimization Strategies	Main Advantages	Limitations	Ref.
Morphological modulation	(1) Increase the specific surface area and improve the exposure of active sites. (2) Optimize mass transfer path and improve reaction rate.	(1) Difficult to control morphology, requiring precise regulation of synthesis conditions. (2) Some forms may be unstable and prone to agglomeration.	[98]
Structural engineering	Constructing specific structures such as core–shell structures and hollow structures to improve stability and activity.	(1) High structural complexity and increased synthesis costs. (2) The structural stability is greatly affected by the preparation process.	[115]
Carbon hybridization	(1) Improve conductivity and promote electron transport. (2) Provide a stable support structure to prevent agglomeration of manganese-based materials.	(1) The selection and composite ratio of carbon materials need to be optimized. (2) Impurities may be introduced during the carbonization process, affecting performance.	[55]
Heterointerface construction	(1) Generates synergistic effects to enhance catalytic activity. (2) Facilitates rapid electron and ion transfer at the interface.	(1) The interface engineering is complex and difficult to control precisely. (2) The stability of the interface is significantly influenced by environmental factors.	[66]
Heteroatom doping	(1) Modulates the electronic structure to optimize adsorption energy. (2) Introduces new active sites, thereby improving catalytic performance.	(1) The type and amount of doping elements need to be precisely controlled. (2) Doping may lead to lattice distortion, affecting the stability of the material.	[19,47]
Defect engineering	(1) Generates defects such as oxygen vacancies to enhance catalytic activity. (2) Modulates the surface electronic structure to optimize reaction pathways.	(1) The type and concentration of defects are difficult to control accurately. (2) Excessive defects may cause structural damage to the material, leading to a decrease in stability.	[56]

By addressing current challenges and advancing the aforementioned research directions, manganese-based electrocatalysts are expected to play a more significant role in the field of rechargeable ZABs, providing strong support for achieving efficient and sustainable green energy storage and conversion. We firmly believe that with continuous research and technological advancements, manganese-based electrocatalysts will exhibit broader application prospects in the future energy landscape.

Author Contributions: Writing—original draft preparation, Z.Y.; writing—review and editing, M.J., T.W. and L.Y. and T.W. All authors have read and agreed to the published version of the manuscript.

Funding: This research was funded by the Distinguished Young Scholar Fund Project of Hunan Province Natural Science Foundation (2025JJ20047, 2023JJ10041), the Hunan Provincial Education Office Foundation of China (22A0114), The Undergraduate Innovation and Entrepreneurship Training

Program Project of Hunan Province (S202410530218), the RSC Research Fund grant (R24-5979269037), and the National Natural Science Foundation of China (52371237).

Data Availability Statement: The figure data will be made available upon request.

Conflicts of Interest: The authors declare no conflicts of interest.

References

- Li, W.; Chen, W.; Zhang, H.; Zhang, Z. Integratable solid-state zinc-air battery with extended cycle life inspired by bionics. *Chem. Eng. J.* **2022**, *435*, 134900. [[CrossRef](#)]
- García-Rodríguez, M.; Cazorla-Amorós, D.; Morallón, E. Eco-Friendly Mechanochemical Synthesis of Bifunctional Metal Oxide Electrocatalysts for Zn-Air Batteries. *ChemSusChem* **2024**, *17*, e202401055. [[CrossRef](#)] [[PubMed](#)]
- Labbe, M.; Clark, M.P.; Cadieu, K.; Ivey, D.G. Bifunctional Mn-Fe Oxide Catalysts for Zn-Air Battery Air Electrodes Fabricated Through Atomic Layer Deposition. *Batter. Supercaps* **2024**, *7*, e202400133. [[CrossRef](#)]
- Xu, H.; Gao, Y.; Li, R.; Sun, W.; Lu, X.; Bai, J.; Yang, P. Manganese, nitrogen co-doped porous carbon with high-loading active sites as the oxygen reduction catalyst for Zn-air batteries. *Sustain. Energy Fuels* **2024**, *8*, 3290–3295. [[CrossRef](#)]
- Wang, Y.; Chu, F.; Zeng, J.; Wang, Q.; Naren, T.; Li, Y.; Cheng, Y.; Lei, Y.; Wu, F. Single Atom Catalysts for Fuel Cells and Rechargeable Batteries: Principles, Advances, and Opportunities. *ACS Nano* **2021**, *15*, 210–239. [[CrossRef](#)]
- Chen, Z.; Wang, Q.; Zhang, X.; Lei, Y.; Hu, W.; Luo, Y.; Wang, Y. N-doped defective carbon with trace Co for efficient rechargeable liquid electrolyte-/all-solid-state Zn-air batteries. *Sci. Bull.* **2018**, *63*, 548–555. [[CrossRef](#)]
- Ambriz-Peláez, O.; Béjar, J.; Delgado, A.D.; Rodríguez-González, C.; Ramos-Castillo, C.M.; Álvarez-Contreras, L.; Guerra-Balcázar, M.; Arjona, N. NiMn layered double hydroxides with promoted surface defects as bifunctional electrocatalysts for rechargeable zinc-air batteries. *FlatChem* **2024**, *45*, 100664. [[CrossRef](#)]
- Zou, X.; Lu, Q.; Tang, M.; Wu, J.; Zhang, K.; Li, W.; Hu, Y.; Xu, X.; Zhang, X.; Shao, Z.; et al. Catalyst-Support Interaction in Polyaniline-Supported Ni₃Fe Oxide to Boost Oxygen Evolution Activities for Rechargeable Zn-Air Batteries. *Nano-Micro Lett.* **2024**, *17*, 6. [[CrossRef](#)]
- Pan, Y.; Li, M.; Mi, W.; Wang, M.; Li, J.; Zhao, Y.; Ma, X.; Wang, B.; Zhu, W.; Cui, Z.; et al. Single-atomic Mn sites coupled with Fe₃C nanoparticles encapsulated in carbon matrixes derived from bimetallic Mn/Fe polyphthalocyanine conjugated polymer networks for accelerating electrocatalytic oxygen reduction. *Nano Res.* **2022**, *15*, 7976–7985. [[CrossRef](#)]
- Wang, Y.; Kumar, A.; Ma, M.; Jia, Y.; Wang, Y.; Zhang, Y.; Zhang, G.; Sun, X.; Yan, Z. Hierarchical peony-like FeCo-NC with conductive network and highly active sites as efficient electrocatalyst for rechargeable Zn-air battery. *Nano Res.* **2020**, *13*, 1090–1099. [[CrossRef](#)]
- Jin, W.; Chen, J.; Liu, B.; Hu, J.; Wu, Z.; Cai, W.; Fu, G. Oxygen Vacancy-Rich In-Doped CoO/CoP Heterostructure as an Effective Air Cathode for Rechargeable Zn-Air Batteries. *Small* **2019**, *15*, 1904210. [[CrossRef](#)]
- Tang, B.; Yang, J.; Kou, Z.; Xu, L.; Seng, H.L.; Xie, Y.; Handoko, A.D.; Liu, X.; Seh, Z.W.; Kawai, H.; et al. Surface-engineered cobalt oxide nanowires as multifunctional electrocatalysts for efficient Zn-Air batteries-driven overall water splitting. *Energy Storage Mater.* **2019**, *23*, 1–7. [[CrossRef](#)]
- Xu, M.; Wei, M. Layered Double Hydroxide-Based Catalysts: Recent Advances in Preparation, Structure, and Applications. *Adv. Funct. Mater.* **2018**, *28*, 1802943. [[CrossRef](#)]
- Li, L.; Li, Y.; Huang, R.; Cao, X.; Wen, Y. Single Mn Atom Anchored on Nitrogen-Doped Graphene as a Highly Efficient Electrocatalyst for Oxygen Reduction Reaction. *Chem. A Eur. J.* **2021**, *27*, 9686–9693. [[CrossRef](#)] [[PubMed](#)]
- Yang, Y.; Sun, C.; Zhang, H.; Ke, S.; Liu, H.; Dou, M.; Wang, F. Bimetal Organic Framework Derived Atomically Dispersed Mn and N Codoped Porous Carbon for Efficient Oxygen Reduction. *Eur. J. Inorg. Chem.* **2021**, *2021*, 4452–4457. [[CrossRef](#)]
- Li, P.; Zhu, C.; Yang, L.; Shi, J.; Hu, W.; Li, Z.; Wu, J.; Wang, H. One single-atom Mn doping strategy enabling two functions of oxygen reduction reaction and pseudocapacitive performance. *Energy Storage Mater.* **2024**, *71*, 103639. [[CrossRef](#)]
- Zong, L.; Lu, F.; Zhang, W.; Fan, K.; Chen, X.; Johannessen, B.; Qi, D.; Bedford, N.M.; Warren, M.; Segre, C.U.; et al. Atomically-dispersed Mn-(N-C₂)₂(O-C₂)₂ sites on carbon for efficient oxygen reduction reaction. *Energy Storage Mater.* **2022**, *49*, 209–218. [[CrossRef](#)]
- Zhong, G.; Zou, L.; Chi, X.; Meng, Z.; Chen, Z.; Li, T.; Huang, Y.; Fu, X.; Liao, W.; Zheng, S.; et al. Atomically dispersed Mn-N_x catalysts derived from Mn-hexamine coordination frameworks for oxygen reduction reaction. *Carbon Energy* **2024**, *6*, e484. [[CrossRef](#)]
- Zhang, X.; Yang, F.; Sun, S.; Wei, K.; Liu, H.; Li, G.; Sun, Y.; Li, X.; Qian, J.; Du, S.; et al. Boosting oxygen reduction via MnP nanoparticles encapsulated by N, P-doped carbon to Mn single atoms sites for Zn-air batteries. *J. Colloid. Interface Sci.* **2024**, *657*, 240–249. [[CrossRef](#)]
- Wang, H.; Kong, Z.; Wang, M.; Huang, B.; Guan, L. Mn-N-C catalysts derived from metal triazole framework with hierarchical porosity for efficient oxygen reduction. *Nanotechnology* **2023**, *34*, 145403. [[CrossRef](#)]

21. Bai, X.; Wang, Y.; Han, J.; Niu, X.; Guan, J. Engineering the electronic structure of isolated manganese sites to improve the oxygen reduction, Zn-air battery and fuel cell performances. *Appl. Catal. B Environ.* **2023**, *337*, 122966. [[CrossRef](#)]
22. Luo, Y.; Wang, Q.; Chen, Y.; Feng, J.; Wang, L.; Jiang, Y.; Li, L.; Xu, X.; Feng, J. Mn–N₃–O-Loaded Graphitic Carbon Aerogel for an Efficient Oxygen Reduction Reaction. *ACS Sustain. Chem. Eng.* **2023**, *11*, 8075–8083. [[CrossRef](#)]
23. Wang, Q.; Tan, Y.; Tang, S.; Liu, W.; Zhang, Y.; Xiong, X.; Lei, Y. Edge-Hosted Mn-N₄-C₁₂ Site Tunes Adsorption Energy for Ultralow-Temperature and High-Capacity Solid-State Zn-Air Battery. *ACS Nano* **2023**, *17*, 9565–9574. [[CrossRef](#)]
24. Li, J.; Zou, S.; Huang, J.; Wu, X.; Lu, Y.; Liu, X.; Song, B.; Dong, D. Mn-N-P doped carbon spheres as an efficient oxygen reduction catalyst for high performance Zn-Air batteries. *Chin. Chem. Lett.* **2023**, *34*, 107222. [[CrossRef](#)]
25. Zhan, X.; Jin, Y.; Gao, Z.; Liu, W.; Zhi, Q.; Chen, B.; Xu, Q.; Jiang, R.; Wang, K.; Sun, T.; et al. Biomass-derived carbon fiber with atomic Mn-N₄ sites for efficient electrocatalytic oxygen reduction reaction. *J. Mater. Sci.* **2022**, *57*, 15943–15953. [[CrossRef](#)]
26. Chen, T.; Huang, Z.; Liu, J.; Jiang, L.; Chu, J.; Song, C.; Kong, A. Mn-Pyridine N site-enriched Mn-N-C derived from covalent organic polymer for electrochemical oxygen reduction and capacitive storage. *Ionics* **2021**, *27*, 5229–5239. [[CrossRef](#)]
27. Chen, Z.; Liao, X.; Sun, C.; Zhao, K.; Ye, D.; Li, J.; Wu, G.; Fang, J.; Zhao, H.; Zhang, J. Enhanced performance of atomically dispersed dual-site Fe-Mn electrocatalysts through cascade reaction mechanism. *Appl. Catal. B Environ.* **2021**, *288*, 120021. [[CrossRef](#)]
28. He, Y.; Li, H.; Wang, Y.; Jia, Y.; Liu, Y.; Tan, Q. Heteroatom anchors Fe-Mn dual-atom catalysts with bi-functional oxygen catalytic activity for low-temperature rechargeable flexible Zn-air batteries. *J. Energy Chem.* **2024**, *90*, 610–620. [[CrossRef](#)]
29. Sarkar, S.; Biswas, A.; Purkait, T.; Das, M.; Kamboj, N.; Dey, R.S. Unravelling the Role of Fe–Mn Binary Active Sites Electrocatalyst for Efficient Oxygen Reduction Reaction and Rechargeable Zn-Air Batteries. *Inorg. Chem.* **2020**, *59*, 5194–5205. [[CrossRef](#)]
30. Chao, G.; Zhang, Y.; Zhang, L.; Zong, W.; Zhang, N.; Xue, T.; Fan, W.; Liu, T.; Xie, Y. Nitrogen-coordinated single-atom catalysts with manganese and cobalt sites for acidic oxygen reduction. *J. Mater. Chem. A* **2022**, *10*, 5930–5936. [[CrossRef](#)]
31. Dey, G.; Jana, R.; Saifi, S.; Kumar, R.; Bhattacharyya, D.; Datta, A.; Sinha, A.S.K.; Aijaz, A. Dual Single-Atomic Co–Mn Sites in Metal–Organic-Framework-Derived N-Doped Nanoporous Carbon for Electrochemical Oxygen Reduction. *ACS Nano* **2023**, *17*, 19155–19167. [[CrossRef](#)]
32. Jiao, Y.; Deng, L.; Liu, D.; Jiao, Y.; Wang, D.; Chen, J.-F. Process intensification for Fe/Mn-nitrogen-doped carbon-based catalysts toward efficient oxygen reduction reaction of Zn-air battery. *Chem. Eng. Sci.* **2022**, *259*, 117811. [[CrossRef](#)]
33. Situ, A.; Zhao, T.; Huang, Y.; Li, P.; Yang, L.; Zhang, Z.; Wang, Z.; Ou, Y.; Guan, X.; Wen, J.; et al. Dual-MOFs-Derived Fe and Mn Species Anchored on Bamboo-like Carbon Nanotubes for Efficient Oxygen Reduction as Electrocatalysts. *Catalysts* **2023**, *13*, 1161. [[CrossRef](#)]
34. Wei, W.; Deng, X.; Zhao, K.; Zhang, M.; Zhou, H.; Wang, W. Dual-metal M-N-C (M = Mn, Co) as an effective oxygen electrocatalyst for zinc-air battery. *J. Alloys Compd.* **2023**, *968*, 172136. [[CrossRef](#)]
35. Liu, H.; Jiang, L.; Khan, J.; Wang, X.; Xiao, J.; Zhang, H.; Xie, H.; Li, L.; Wang, S.; Han, L. Decorating Single-Atomic Mn Sites with FeMn Clusters to Boost Oxygen Reduction Reaction. *Angew. Chem. Int. Ed.* **2022**, *62*, e202214988. [[CrossRef](#)]
36. Sun, R.-M.; Yao, Y.-Q.; Wang, A.-J.; Fang, K.-M.; Zhang, L.; Feng, J.-J. One-step pyrolysis synthesis of nitrogen, manganese-codoped porous carbon encapsulated cobalt-iron nanoparticles with superior catalytic activity for oxygen reduction reaction. *J. Colloid. Interface Sci.* **2021**, *592*, 405–415. [[CrossRef](#)] [[PubMed](#)]
37. Tian, H.; Cui, X.; Dong, H.; Meng, G.; Kong, F.; Chen, Y.; Peng, L.; Chen, C.; Chang, Z.; Shi, J. Engineering single MnN₄ atomic active sites on polydopamine-modified helical carbon tubes towards efficient oxygen reduction. *Energy Storage Mater.* **2021**, *37*, 274–282. [[CrossRef](#)]
38. Guo, X.; Xue, S.; Zhang, X.; Qin, J.; Hong, M.; Chen, Q.; Liu, W.; Du, C.; Chen, J. Mn atomic clusters and Fe nanoparticles in-situ confined nitrogen carbon nanotubes for efficient and durable ORR electrocatalysts in both alkaline and acidic media. *J. Alloys Compd.* **2023**, *953*, 169992. [[CrossRef](#)]
39. Zhao, S.; Ma, Z.; Wan, Z.; Li, J.; Wang, X. Noble-Metal-Free FeMn-N-C catalyst for efficient oxygen reduction reaction in both alkaline and acidic media. *J. Colloid. Interface Sci.* **2023**, *642*, 800–809. [[CrossRef](#)]
40. Cui, T.; Wang, Y.P.; Ye, T.; Wu, J.; Chen, Z.; Li, J.; Lei, Y.; Wang, D.; Li, Y. Engineering Dual Single-Atom Sites on 2D Ultrathin N-doped Carbon Nanosheets Attaining Ultra-Low-Temperature Zinc-Air Battery. *Angew. Chem. Int. Ed.* **2022**, *61*, e202115219. [[CrossRef](#)]
41. Zhang, X.; Du, K.; Wang, H.; Li, Z.; Zhang, G. Atomic ternary-doped MnCoZn-N-C for efficient oxygen electroreduction. *J. Energy Storage* **2023**, *72*, 108508. [[CrossRef](#)]
42. Wang, X.; Zhang, J.; Ma, D.; Feng, X.; Wang, L.; Wang, B. Metal–Organic Framework-Derived Trimetallic Nanocomposites as Efficient Bifunctional Oxygen Catalysts for Zinc–Air Batteries. *ACS Appl. Mater. Interfaces* **2021**, *13*, 33209–33217. [[CrossRef](#)]
43. Zhou, Q.; Hou, S.; Cheng, Y.; Sun, R.; Shen, W.; Tian, R.; Yang, J.; Pang, H.; Xu, L.; Huang, K.; et al. Interfacial engineering Co and MnO within N,S co-doped carbon hierarchical branched superstructures toward high-efficiency electrocatalytic oxygen reduction for robust Zn-air batteries. *Appl. Catal. B Environ.* **2021**, *295*, 120281. [[CrossRef](#)]

44. Sun, C.; Zhu, E.; Shi, C.; Yu, J.; Yin, S.; Liu, C.; Cui, X.; Liu, W.; Xu, M. High-performance MnO/N-rGO catalyst for half-cell and Zn-air batteries by photochemically assisted synthesis. *Ceram. Int.* **2023**, *49*, 13972–13981. [CrossRef]
45. Zhou, W.; Liu, Y.; Wu, D.; Zhang, P.; Zhang, G.; Sun, K.; Li, B.; Jiang, J. Co@C,MnO-NAC via selective wrapping for effective oxygen electrocatalysis in rechargeable Zn-air batteries. *Sustain. Energy Fuels* **2022**, *6*, 791–799. [CrossRef]
46. Peng, L.; Peng, X.; Zhu, Z.; Xu, Q.; Luo, K.; Ni, Z.; Yuan, D. Efficient MnO and Co nanoparticles coated with N-doped carbon as a bifunctional electrocatalyst for rechargeable Zn-air batteries. *Int. J. Hydrogen Energy* **2023**, *48*, 19126–19136. [CrossRef]
47. Ruan, Y.; Lei, H.; Xue, W.; Wang, T.; Song, S.; Xu, H.; Yu, Y.; Zhang, G.-R.; Mei, D. Cu-N-C assisted MnO nanorods as bifunctional electrocatalysts for superior long-cycle Zn-air batteries. *J. Alloys Compd.* **2023**, *934*, 167781. [CrossRef]
48. Qian, J.; Guo, X.; Wang, T.; Liu, P.; Zhang, H.; Gao, D. Bifunctional porous Co-doped NiO nanoflowers electrocatalysts for rechargeable zinc-air batteries. *Appl. Catal. B Environ.* **2019**, *250*, 71–77. [CrossRef]
49. Tian, Y.; Zhao, H.; Wang, X. Make the chemical industry greener with green carbon science: An interview with Mingyuan He. *GreenChE* **2020**, *1*, 3–4. [CrossRef]
50. Ji, D.; Sun, J.; Tian, L.; Chinnappan, A.; Zhang, T.; Jayathilaka, W.A.D.M.; Gosh, R.; Baskar, C.; Zhang, Q.; Ramakrishna, S. Engineering of the Heterointerface of Porous Carbon Nanofiber-Supported Nickel and Manganese Oxide Nanoparticle for Highly Efficient Bifunctional Oxygen Catalysis. *Adv. Funct. Mater.* **2020**, *30*, 1910568. [CrossRef]
51. Yan, G.; Lian, Y.; Gu, Y.; Yang, C.; Sun, H.; Mu, Q.; Li, Q.; Zhu, W.; Zheng, X.; Chen, M.; et al. Phase and Morphology Transformation of MnO₂ Induced by Ionic Liquids toward Efficient Water Oxidation. *ACS Catal.* **2018**, *8*, 10137–10147. [CrossRef]
52. Ni, S.; Zhang, H.; Zhao, Y.; Li, X.; Sun, Y.; Qian, J.; Xu, Q.; Gao, P.; Wu, D.; Kato, K.; et al. Single atomic Ag enhances the bifunctional activity and cycling stability of MnO₂. *Chem. Eng. J.* **2019**, *366*, 631–638. [CrossRef]
53. Xu, N.; Zhang, Y.; Wang, Y.; Wang, M.; Su, T.; Coco, C.A.; Qiao, J.; Zhou, X.-D. Hierarchical bifunctional catalysts with tailored catalytic activity for high-energy rechargeable Zn-air batteries. *Appl. Energy* **2020**, *279*, 115876. [CrossRef]
54. Meng, Y.; Song, W.; Huang, H.; Ren, Z.; Chen, S.-Y.; Suib, S.L. Structure-Property Relationship of Bifunctional MnO₂ Nanostructures: Highly Efficient, Ultra-Stable Electrochemical Water Oxidation and Oxygen Reduction Reaction Catalysts Identified in Alkaline Media. *JACS* **2014**, *136*, 11452–11464. [CrossRef] [PubMed]
55. Zhao, H.; Jiang, R.; Zhang, Y.; Xie, B.; Fu, J.; Yuan, X.; Yang, W.; Wu, Y.; Zhang, R. An MnO₂ nanosheet@nitrogen-doped graphene aerogel enables high specific energy and high specific power for supercapacitors and Zn-air batteries. *J. Mater. Chem. A* **2021**, *9*, 5848–5856. [CrossRef]
56. Zhou, B.; Xu, N.; Lu, T.; Wang, Y.; Lou, S.; Cai, D.; Wu, L.; Yang, W.; Liu, G.; Lee, J.K.; et al. Dual-Carbon Assisted Oxygen Vacancy Engineering for Optimizing Mn(III) Sites to Enhance Zn-air Battery Performances. *Adv. Funct. Mater.* **2024**, *35*, 2414269. [CrossRef]
57. Chai, H.; Wei, M.; Su, Y.; Wang, Y.; Jia, D.; Sun, Z.; Zhou, W. Facile Controlled Growth of Podetium-Like MnO₂ Crystals and the Catalytic Effect of MnO₂/N-Doped Graphene on the Oxygen Reduction Reaction. *Eur. J. Inorg. Chem.* **2018**, *2018*, 1315–1321. [CrossRef]
58. Ou, X.; Li, Q.; Xu, D.; Guo, J.; Yan, F. In Situ Growth of MnO₂ Nanosheets on N-Doped Carbon Nanotubes Derived from Polypyrrole Tubes for Supercapacitors. *Chem. Asian J.* **2018**, *13*, 545–551. [CrossRef] [PubMed]
59. Zheng, X.; Zuria, A.M.; Mohamedi, M. Free-Standing Tunnel-Structured MnO₂ Nanorods-Doped with Nickel and Cobalt Cations as Bifunctional Electrocatalysts for Zn-Air Batteries. *Adv. Mater. Technol.* **2023**, *8*, 2301142. [CrossRef]
60. Wang, Y.; Qiao, M.; Qiao, L.; Shi, K. Molten salt method for preparing Mn_{0.3}Ru_{0.7}O₂ nanosheets as a superior bifunctional catalyst for rechargeable zinc-air batteries. *J. Power Sources* **2024**, *622*, 235367. [CrossRef]
61. Li, T.; Hu, Y.; Liu, K.; Yin, J.; Li, Y.; Fu, G.; Zhang, Y.; Tang, Y. Hollow yolk-shell nanoboxes assembled by Fe-doped Mn₃O₄ nanosheets for high-efficiency electrocatalytic oxygen reduction in Zn-Air battery. *Chem. Eng. J.* **2022**, *427*, 131992. [CrossRef]
62. Huang, Z.; Qin, X.; Gu, X.; Li, G.; Mu, Y.; Wang, N.; Ithisuphalap, K.; Wang, H.; Guo, Z.; Shi, Z.; et al. Mn₃O₄ Quantum Dots Supported on Nitrogen-Doped Partially Exfoliated Multiwall Carbon Nanotubes as Oxygen Reduction Electrocatalysts for High-Performance Zn-Air Batteries. *ACS Appl. Mater. Interfaces* **2018**, *10*, 23900–23909. [CrossRef]
63. Li, L.; Yang, J.; Yang, H.; Zhang, L.; Shao, J.; Huang, W.; Liu, B.; Dong, X. Anchoring Mn₃O₄ Nanoparticles on Oxygen Functionalized Carbon Nanotubes as Bifunctional Catalyst for Rechargeable Zinc-Air Battery. *ACS Appl. Energy Mater.* **2018**, *1*, 963–969. [CrossRef]
64. Dong, M.; Liu, X.; Jiang, L.; Zhu, Z.; Shu, Y.; Chen, S.; Dou, Y.; Liu, P.; Yin, H.; Zhao, H. Cobalt-doped Mn₃O₄ nanocrystals embedded in graphene nanosheets as a high-performance bifunctional oxygen electrocatalyst for rechargeable Zn-Air batteries. *Green. Energy Env.* **2020**, *5*, 499–505. [CrossRef]
65. Wang, W.; Chen, J.-Q.; Tao, Y.-R.; Zhu, S.-N.; Zhang, Y.-X.; Wu, X.-C. Flowerlike Ag-Supported Ce-Doped Mn₃O₄ Nanosheet Heterostructure for a Highly Efficient Oxygen Reduction Reaction: Roles of Metal Oxides in Ag Surface States. *ACS Catal.* **2019**, *9*, 3498–3510. [CrossRef]
66. Huang, Q.; Zhong, X.; Zhang, Q.; Wu, X.; Jiao, M.; Chen, B.; Sheng, J.; Zhou, G. Co₃O₄/Mn₃O₄ hybrid catalysts with heterointerfaces as bifunctional catalysts for Zn-air batteries. *J. Energy Chem.* **2022**, *68*, 679–687. [CrossRef]

67. Wang, P.; Zhang, S.; Wang, Z.; Mo, Y.; Luo, X.; Yang, F.; Lv, M.; Li, Z.; Liu, X. Manganese-based oxide electrocatalysts for the oxygen evolution reaction: A review. *J. Mater. Chem. A* **2023**, *11*, 5476–5494. [[CrossRef](#)]
68. Akbarian, P.; Kheirmand, M. Efficient and Stable Dual-Active-Site of Core-Shell NiFe-Layered Double Hydroxide Anchored on FeMnON-N-Doped Carbon Nanotubes as Bifunctional Oxygen Electrocatalysts for Zn-Air Batteries. *J. Electrochem. Soc.* **2024**, *171*, 020514. [[CrossRef](#)]
69. Wu, L.; Zhao, R.; Du, G.; Wang, H.; Hou, M.; Zhang, W.; Sun, P.; Chen, T. Hierarchically porous Fe/N/S/C nanospheres with high-content of Fe-Nx for enhanced ORR and Zn-air battery performance. *Green. Energy Environ.* **2023**, *8*, 1693–1702. [[CrossRef](#)]
70. Liu, B.; Wang, X.; Wang, R.; Zhang, G.; Xu, X.; Liu, J.; Sun, Z.; Liu, M.; Wang, C.; Meng, X.; et al. Activating and stabilizing Co sites in CoP for triggering oxygen electrocatalysis in zinc-air battery. *Chem. Eng. J.* **2023**, *475*, 146154. [[CrossRef](#)]
71. Miao, W.; Cao, X.; Qin, M.; Lv, E.; Yu, H.; Zhang, X.; Dong, X. N-doping FeNi@C(Nx) core-shell nanoparticles synthesized by arc plasma as a highly efficient bifunctional electrocatalyst for all-solid zinc-air batteries. *Compos. Part. B-Eng.* **2023**, *260*, 110769. [[CrossRef](#)]
72. Ma, X.; Liu, M.; Xu, Z.; Qiao, P.; Li, Q.; Wang, R.; Zhang, S.; Zou, J.; Jiang, B. Heterointerface engineering of yolk-shell-structured Mn₂O₃/RuO₂ for boosting oxygen electrocatalysis in rechargeable liquid and flexible zinc-air batteries. *Chem. Eng. J.* **2024**, *498*, 155118. [[CrossRef](#)]
73. Shao, C.; Liao, F.; Zhu, W.; Zhang, Y.; Ma, M.; Yang, J.; Yin, K.; Shao, M.; Jiang, B. Carbon dots bridge NiO and Mn₂O₃ as highly efficient bifunctional oxygen electrocatalysts for rechargeable zinc-air batteries. *Appl. Surf. Sci.* **2022**, *596*, 153642. [[CrossRef](#)]
74. Kim, H.; Min, K.; Shim, S.E.; Lim, D.; Baeck, S.-H. Ni-doped Mn₂O₃ microspheres as highly efficient electrocatalyst for oxygen reduction reaction and Zn-air battery. *Int. J. Hydrogen Energy* **2022**, *47*, 2378–2388. [[CrossRef](#)]
75. Gu, Y.; Yan, G.; Lian, Y.; Qi, P.; Mu, Q.; Zhang, C.; Deng, Z.; Peng, Y. MnIII-enriched α -MnO₂ nanowires as efficient bifunctional oxygen catalysts for rechargeable Zn-air batteries. *Energy Storage Mater.* **2019**, *23*, 252–260. [[CrossRef](#)]
76. Wang, F.; Zhao, H.; Ma, Y.; Yang, Y.; Li, B.; Cui, Y.; Guo, Z.; Wang, L. Core-shell-structured Co@Co₄N nanoparticles encapsulated into MnO-modified porous N-doping carbon nanocubes as bifunctional catalysts for rechargeable Zn-air batteries. *J. Energy Chem.* **2020**, *50*, 52–62. [[CrossRef](#)]
77. Zhu, X.; Wang, J.; Chai, L.; Tang, G.; Wan, K.; Pan, J. A new Mn_xO_y/carbon nanorods derived from bimetallic Zn/Mn metal-organic framework as an efficient oxygen reduction reaction electrocatalyst for alkaline Zn-Air batteries. *J. Solid State Electrochem.* **2022**, *26*, 1163–1173. [[CrossRef](#)]
78. Tian, H.; Zeng, L.; Huang, Y.; Ma, Z.; Meng, G.; Peng, L.; Chen, C.; Cui, X.; Shi, J. In Situ Electrochemical Mn(III)/Mn(IV) Generation of Mn(II)O Electrocatalysts for High-Performance Oxygen Reduction. *Nano-Micro Lett.* **2020**, *12*, 161. [[CrossRef](#)]
79. Clark, M.P.; Xiong, M.; Cadien, K.; Ivey, D.G. High Performance Oxygen Reduction/Evolution Electrodes for Zinc–Air Batteries Prepared by Atomic Layer Deposition of MnOx. *ACS Appl. Energy Mater.* **2019**, *3*, 603–613. [[CrossRef](#)]
80. Varignon, J.; Bibes, M.; Zunger, A. Origin of band gaps in 3d perovskite oxides. *Nat. Commun.* **2019**, *10*, 1658. [[CrossRef](#)]
81. Zheng, Y.; Zhang, R.; Zhang, L.; Gu, Q.; Qiao, Z.A. A Resol-Assisted Cationic Coordinative Co-assembly Approach to Mesoporous ABO₃ Perovskite Oxides with Rich Oxygen Vacancy for Enhanced Hydrogenation of Furfural to Furfuryl Alcohol. *Angew. Chem. Int. Ed.* **2021**, *60*, 4774–4781. [[CrossRef](#)]
82. Zheng, Y.; Wang, L.; Liu, H.; Yang, J.; Zhang, R.; Zhang, L.; Qiao, Z.A. A Modular Co-assembly Strategy for Ordered Mesoporous Perovskite Oxides with Abundant Surface Active Sites. *Angew. Chem. Int. Ed.* **2022**, *61*, e202209038. [[CrossRef](#)] [[PubMed](#)]
83. Yuan, R.-h.; Chen, B.; Zhang, Y.; Tan, F.; Liu, T. Boosting the bifunctional electrocatalytic activity of cobalt free perovskite oxide (La_{0.8}Sr_{0.2})_{0.95}MnO₃ via iron doping for high-efficiency Zn-air batteries. *Sep. Purif. Technol.* **2022**, *300*, 121858. [[CrossRef](#)]
84. Xu, X.; Wang, W.; Zhou, W.; Shao, Z. Recent Advances in Novel Nanostructuring Methods of Perovskite Electrocatalysts for Energy-Related Applications. *Small Methods* **2018**, *2*, 1800071. [[CrossRef](#)]
85. Xu, X.; Su, C.; Shao, Z. Fundamental Understanding and Application of Ba_{0.5}Sr_{0.5}Co_{0.8}Fe_{0.2}O₃– δ Perovskite in Energy Storage and Conversion: Past, Present, and Future. *Energy Fuels* **2021**, *35*, 13585–13609. [[CrossRef](#)]
86. Kuai, L.; Kan, E.; Cao, W.; Huttula, M.; Ollikkala, S.; Ahopelto, T.; Honkanen, A.-P.; Huotari, S.; Wang, W.; Geng, B. Mesoporous LaMnO_{3+ δ} perovskite from spray–pyrolysis with superior performance for oxygen reduction reaction and Zn–air battery. *Nano Energy* **2018**, *43*, 81–90. [[CrossRef](#)]
87. Shui, Z.; Tian, H.; Yu, S.; Xiao, H.; Zhao, W.; Chen, X. La_{0.75}Sr_{0.25}MnO₃-based perovskite oxides as efficient and durable bifunctional oxygen electrocatalysts in rechargeable Zn-air batteries. *Sci. China Mater.* **2022**, *66*, 1002–1012. [[CrossRef](#)]
88. Zhang, Y.; Feng, F.; Zhang, C.; Zheng, Q.; Wang, C.; Hu, H.; Wu, M.; Guo, Y. Enhanced Catalytic Activity of LaMnO₃ by A-Site Substitution as Air Electrode of Zn–Air Batteries with Attractive Durability. *Energy Fuels* **2020**, *34*, 10170–10177. [[CrossRef](#)]
89. Flores-Lasluisa, J.X.; García-Rodríguez, M.; Cazorla-Amorós, D.; Morallón, E. In-situ synthesis of encapsulated N-doped carbon metal oxide nanostructures for Zn-air battery applications. *Carbon* **2024**, *225*, 119147. [[CrossRef](#)]
90. Shi, W.; Dong, X.; Luo, Y.; Wang, R.; Wang, G.; Chen, J.; Liu, C.; Zhang, J. Regulation of the B Site at La(Ni_{0.1})MnO₃ Perovskite Decorated with N-Doped Carbon for a Bifunctional Electrocatalyst in Zn–Air Batteries. *Ind. Eng. Chem. Res.* **2023**, *62*, 2687–2697. [[CrossRef](#)]

91. Yan, L.; Lin, Y.; Yu, X.; Xu, W.; Salas, T.; Smallidge, H.; Zhou, M.; Luo, H. La_{0.8}Sr_{0.2}MnO₃-Based Perovskite Nanoparticles with the A-Site Deficiency as High Performance Bifunctional Oxygen Catalyst in Alkaline Solution. *ACS Appl. Mater. Interfaces* **2017**, *9*, 23820–23827. [CrossRef]
92. Miao, H.; Wang, Z.; Wang, Q.; Sun, S.; Xue, Y.; Wang, F.; Zhao, J.; Liu, Z.; Yuan, J. A new family of Mn-based perovskite (La_{1-x}Y_xMnO₃) with improved oxygen electrocatalytic activity for metal-air batteries. *Energy* **2018**, *154*, 561–570. [CrossRef]
93. Shui, Z.; Tian, H.; Raza, M.A.; Zhu, L.; Zhao, W.; Chen, X. Advanced Zn-air batteries based on efficient and durable perovskite/dual-doped graphene bifunctional oxygen catalysts. *J. Alloys Compd.* **2023**, *939*, 168817. [CrossRef]
94. Stoerzinger, K.A.; Risch, M.; Han, B.; Shao-Horn, Y. Recent Insights into Manganese Oxides in Catalyzing Oxygen Reduction Kinetics. *ACS Catal.* **2015**, *5*, 6021–6031. [CrossRef]
95. Yang, C.; Grimaud, A. Factors Controlling the Redox Activity of Oxygen in Perovskites: From Theory to Application for Catalytic Reactions. *Catalysts* **2017**, *7*, 149. [CrossRef]
96. Liu, W.; Su, Q.; Yu, L.; Du, G.; Li, C.; Zhang, M.; Ding, S.; Xu, B. Understanding reaction mechanism of oxygen evolution reaction using Ru single atoms as catalyst for Li-O₂ battery. *J. Alloys Compd.* **2021**, *886*, 161189. [CrossRef]
97. Li, X.X.; Wang, Y.; Li, Y.C.; Liang, Y. Durable bifunctional electrocatalyst for cathode of zinc-air battery: Surface pre-reconstruction of La_{0.7}Sr_{0.3}MnO₃ perovskite by iron ions. *J. Alloys Compd.* **2024**, *976*, 173398. [CrossRef]
98. Dai, Y.; Yu, J.; Zhang, Z.; Zhai, S.; Cheng, C.; Zhao, S.; Tan, P.; Shao, Z.; Ni, M. Regulating the Interfacial Electron Density of La_{0.8}Sr_{0.2}Mn_{0.5}Co_{0.5}O₃/RuO_x for Efficient and Low-Cost Bifunctional Oxygen Electrocatalysts and Rechargeable Zn-Air Batteries. *ACS Appl. Mater. Interfaces* **2021**, *13*, 61098–61106. [CrossRef]
99. Moon, G.H.; Yu, M.; Chan, C.K.; Tüysüz, H. Highly Active Cobalt-Based Electrocatalysts with Facile Incorporation of Dopants for the Oxygen Evolution Reaction. *Angew. Chem. Int. Ed.* **2019**, *58*, 3491–3495. [CrossRef]
100. Alegre, C.; Busacca, C.; Di Blasi, A.; Cannilla, C.; Barbera, O.; Antonucci, V.; Lázaro, M.J.; Baglio, V. Electrospun MnCo₂O₄/carbon-nanofibers as oxygen electrode for alkaline zinc-air batteries. *J. Energy Storage* **2022**, *55*, 105404. [CrossRef]
101. Li, J.; He, X.; Du, Y.; Jiang, M.; Hu, Q.; Yin, J.; Yang, F.; Zhang, J. Superior bifunctional oxygen electrocatalysts based on Co₂MnO₄ with mixed site occupancy, Mn-rich surfaces and twin defects. *Chem. Eng. J.* **2023**, *475*, 146183. [CrossRef]
102. Liu, W.; Bao, J.; Xu, L.; Guan, M.; Lei, Y. Chromium-modulated multifunctional electrocatalytic activities of spinel oxide for Zn-air batteries and overall water splitting. *J. Power Sources* **2020**, *479*, 229099. [CrossRef]
103. Chen, B.; Miao, H.; Yin, M.; Hu, R.; Xia, L.; Zhang, C.; Yuan, J. Mn-based spinels evolved from layered manganese dioxides at mild temperature for the robust flexible quasi-solid-state zinc-air batteries. *Chem. Eng. J.* **2021**, *417*, 129179. [CrossRef]
104. Kosasang, S.; Gatemala, H.; Ma, N.; Chomkhuntod, P.; Sawangphruk, M. Trimetallic Spinel-Type Cobalt Nickel-Doped Manganese Oxides as Bifunctional Electrocatalysts for Zn-Air Batteries. *Batter. Supercaps* **2020**, *3*, 631–637. [CrossRef]
105. Sasidharachari, K.; Cho, K.Y.; Yoon, S. Mesoporous ZnMn₂O₄ Nanospheres as a Nonprecious Bifunctional Catalyst for Zn–Air Batteries. *ACS Appl. Energy Mater.* **2020**, *3*, 3293–3301. [CrossRef]
106. Béjar, J.; Delgado, A.D.; Espinosa-Magaña, F.; Aguilar-Elguezabal, A.; Guerra-Balcázar, M.; Arjona, N.; Álvarez-Contreras, L. Electrodeposition of small sized NiM₂O₄ spinels (M: Co, Mn) as bifunctional nanomaterials for rechargeable zinc-air batteries. *J. Alloys Compd.* **2022**, *929*, 167266. [CrossRef]
107. Balqis, F.; Irmawati, Y.; Geng, D.; Nugroho, F.A.A.; Sumboja, A. Nanostructured Ball-Milled Ni–Co–Mn Oxides from Spent Li-Ion Batteries as Electrocatalysts for Oxygen Evolution Reaction. *ACS Appl. Nano Mater.* **2023**, *7*, 18138–18145. [CrossRef]
108. Zou, J.; Chen, B.; Li, B.; Yin, M.; Miao, H.; Wang, F.; Zhang, C.; Zhang, H.; Yuan, J. Achieving high energy efficiency of alkaline hybrid zinc battery by using the optimized Co–Mn spinel cathode. *Int. J. Hydrogen Energy* **2022**, *47*, 27470–27480. [CrossRef]
109. Wang, Z.; Huang, J.; Wang, L.; Liu, Y.; Liu, W.; Zhao, S.; Liu, Z.Q. Cation-Tuning Induced d-Band Center Modulation on Co-Based Spinel Oxide for Oxygen Reduction/Evolution Reaction. *Angew. Chem. Int. Ed.* **2022**, *61*, e202114696. [CrossRef]
110. Wang, Z.; Wu, P.; Zou, X.; Wang, S.; Du, L.; Ouyang, T.; Liu, Z.Q. Optimizing the Oxygen-Catalytic Performance of Zn–Mn–Co Spinel by Regulating the Bond Competition at Octahedral Sites. *Adv. Funct. Mater.* **2023**, *33*, 2214275. [CrossRef]
111. Béjar, J.; Espinosa-Magaña, F.; Guerra-Balcázar, M.; Ledesma-García, J.; Álvarez-Contreras, L.; Arjona, N.; Arriaga, L.G. Three-Dimensional-Order Macroporous AB₂O₄ Spinels (A, B =Co and Mn) as Electrodes in Zn–Air Batteries. *ACS Appl. Mater. Interfaces* **2020**, *12*, 53760–53773. [CrossRef]
112. Li, J.-G.; Sun, H.; Lv, L.; Li, Z.; Ao, X.; Xu, C.; Li, Y.; Wang, C. Metal–Organic Framework-Derived Hierarchical (Co,Ni)Se₂@NiFe LDH Hollow Nanocages for Enhanced Oxygen Evolution. *ACS Appl. Mater. Interfaces* **2019**, *11*, 8106–8114. [CrossRef] [PubMed]
113. Reddy, D.A.; Reddy, K.A.J.; Gopannagari, M.; Kim, Y.; Rangappa, A.P.; Kumar, D.P.; Kim, T.K. Exposure of NiFe-LDH active sites by cation–exchange to promote photoelectrochemical water splitting performance. *Appl. Surf. Sci.* **2021**, *570*, 151134. [CrossRef]
114. Chala, S.A.; Tsai, M.-C.; Su, W.-N.; Ibrahim, K.B.; Thirumalraj, B.; Chan, T.-S.; Lee, J.-F.; Dai, H.; Hwang, B.-J. Hierarchical 3D Architectured Ag Nanowires Shelled with NiMn-Layered Double Hydroxide as an Efficient Bifunctional Oxygen Electrocatalyst. *ACS Nano* **2020**, *14*, 1770–1782. [CrossRef] [PubMed]
115. Liu, Z.; Yu, C.; Han, X.; Yang, J.; Zhao, C.; Huang, H.; Qiu, J. CoMn Layered Double Hydroxides/Carbon Nanotubes Architectures as High-Performance Electrocatalysts for the Oxygen Evolution Reaction. *ChemElectroChem* **2016**, *3*, 906–912. [CrossRef]

116. Li, K.; Guo, D.; Kang, J.; Wei, B.; Zhang, X.; Chen, Y. Hierarchical Hollow Spheres Assembled with Ultrathin CoMn Double Hydroxide Nanosheets as Trifunctional Electrocatalyst for Overall Water Splitting and Zn Air Battery. *ACS Sustain. Chem. Eng.* **2018**, *6*, 14641–14651. [[CrossRef](#)]
117. Beltran-Huarac, J.; Resto, O.; Carpena-Nuñez, J.; Jadwisienczak, W.M.; Fonseca, L.F.; Weiner, B.R.; Morell, G. Single-Crystal γ -MnS Nanowires Conformally Coated with Carbon. *ACS Appl. Mater. Interfaces* **2014**, *6*, 1180–1186. [[CrossRef](#)]
118. Chen, Y.; Xu, C.; Hou, Z.; Zhou, M.; He, B.; Wang, W.; Ren, W.; Liu, Y.; Chen, L.; Xu, W. 3D N, S-co-doped carbon nanotubes/graphene/MnS ternary hybrid derived from Hummers' method for highly efficient oxygen reduction reaction. *Mater. Today Energy* **2020**, *16*, 100402. [[CrossRef](#)]
119. Rui, X.; Tan, H.; Yan, Q. Nanostructured metal sulfides for energy storage. *Nanoscale* **2014**, *6*, 9889–9924. [[CrossRef](#)]
120. Wang, K.; Wang, Z.; Liu, Y.; Liu, J.; Cui, Z.; Zhang, X.; Ciucci, F.; Tang, Z. Tailoring the interfacial active center of $\text{MnS}_{x}\text{O}_{2-x}/\text{MnCo}_2\text{S}_4$ heterostructure to boost the performance for oxygen evolution reaction and Zn-Air batteries in neutral electrolyte. *Chem. Eng. J.* **2022**, *427*, 131966. [[CrossRef](#)]
121. Chen, K.; Wang, X.; Zhang, C.; Xu, R.; Wang, H.; Chu, L.; Huang, M. Three-phases Co/Co₉S₈/MnS heterostructures engineering for boosted ORR/OER activities in Zn-air batteries. *Mater. Today Energy* **2022**, *30*, 101150. [[CrossRef](#)]
122. Rao, Y.; Li, W.; Chen, S.; Yue, Q.; Zhang, Y.; Kang, Y. V₂O₃/MnS Arrays as Bifunctional Air Electrode for Long-Lasting and Flexible Rechargeable Zn-Air Batteries. *Small* **2022**, *18*, 2104411. [[CrossRef](#)] [[PubMed](#)]
123. Chen, Z.; Duan, X.; Wei, W.; Wang, S.; Ni, B.-J. Recent advances in transition metal-based electrocatalysts for alkaline hydrogen evolution. *J. Mater. Chem. A* **2019**, *7*, 14971–15005. [[CrossRef](#)]
124. Dutta, S.; Indra, A.; Feng, Y.; Han, H.; Song, T. Promoting electrocatalytic overall water splitting with nanohybrid of transition metal nitride-oxynitride. *Appl. Catal. B Environ.* **2019**, *241*, 521–527. [[CrossRef](#)]
125. Davari, E.; Ivey, D.G. Synthesis and electrochemical performance of manganese nitride as an oxygen reduction and oxygen evolution catalyst for zinc-air secondary batteries. *J. Appl. Electrochem.* **2017**, *47*, 815–827. [[CrossRef](#)]
126. Hopkins, B.J.; Chervin, C.N.; Parker, J.F.; Long, J.W.; Rolison, D.R. An Areal-Energy Standard to Validate Air-Breathing Electrodes for Rechargeable Zinc–Air Batteries. *Adv. Energy Mater.* **2020**, *10*, 2001287. [[CrossRef](#)]

Disclaimer/Publisher's Note: The statements, opinions and data contained in all publications are solely those of the individual author(s) and contributor(s) and not of MDPI and/or the editor(s). MDPI and/or the editor(s) disclaim responsibility for any injury to people or property resulting from any ideas, methods, instructions or products referred to in the content.